Precambrian fault reactivation revealed by structural and K-Ar geochronological data from the spent nuclear fuel repository in Olkiluoto, southwestern Finland

Nicklas Nordbäck [a,b,*], Jussi Mattila [c,b], Horst Zwingmann [d], Giulio Viola [e]

[a] Geological Survey of Finland, P.O. Box 96, 02151 Espoo, Finland
[b] University of Turku, Department of Geography and Geology, 20014 Turku, Finland
[c] Rock Mechanics Consulting Finland Oy (RMCF), Vantaankoskentie 14, 01670 Vantaa, Finland
[d] Department of Geology and Mineralogy, Graduate School of Science, Kyoto University, Sakyo-ku, 606-8502 Kyoto, Japan
[e] Dipartimento di Scienze Biologiche, Geologiche e Ambientali, Università di Bologna, Via Zamboni 67, 40126 Bologna, Italy

ARTICLE INFO

ABSTRACT

Integrated structural/geochronological studies help unraveling complex brittle deformation histories. We have analysed the structural geological database of brittle faults from the ONKALO™ underground facility for spent nuclear fuel in Olkiluoto in southwestern Finland. Based on the structural geological data from eleven representative fault zones, we classify the Olkiluoto brittle structural features into four fault systems, referred to as Fault system I to IV. The classification is based on their structural properties and tectonic history, crosscutting relationships, fault rock mineralogical characterization and 3D modelling. Some constraints on the timing of faulting are provided by K-Ar dates on synkinematic illite from fault gouge samples. Our results show that the bedrock in southwestern Finland experienced numerous brittle deformation phases between ca. 1.75 and 0.9 Ga. N-S strike-slip faults (Fault systems I and II) formed at mid-crustal levels ca. 1.79–1.75 Ga ago in response to NW-SE/NNW-SSE compression soon after the Svecofennian orogeny. Later *E*-W striking oblique dextral/normal faults (Fault system III) are tentatively associated with the Gothian orogeny 1.6 Ga ago. These three fault systems were reactivated during NE-SW compression ca. 1.3–1.2 Ga ago, coeval with intrusion of a regional swarm of olivine diabase sills. *E*-W compression at the onset of the Sveconorwegian orogeny ca. 1.1–1.0 Ga ago resulted in the formation of SE dipping low-angle thrust faults (Fault system IV) and the selective reactivation of fault system II and III. Overall E-W extension during the collapse of the Sveconorwegian orogen ca. 0.97–0.87 Ga ago caused the localised reactivation of fault systems III and IV. Our research approach, which is integral to the siting process of repositories for spent nuclear fuel, demonstrates that the basement in southwestern Finland experienced repeated reactivation since the Mesoproterozoic, suggesting that future deformation localization is likely to be also accommodated by reactivation of existing brittle structures rather than formation of new faults.

1. Introduction

Fractures and faults, in addition to representing mechanical discontinuities that act as pathways for fluid flow in low permeability rock volumes such as crystalline basement rocks (e.g., Brace, 1980; Barton et al., 1995; Mattila and Tammisto, 2012; Bense et al., 2013; Marchesini et al., 2019), may also significantly affect the stability of underground rock masses. Repeated deformation through time may reactivate favourably oriented existing discontinuities and cause multiple slip events. The likelihood of reactivations to occur is dependent on the prevailing stress field, the orientation of the fault and the strength of the fault surface (Sibson, 1985; Morris et al., 1996). Consequently, the geometry and the mechanical properties of geological brittle structures need to be systematically studied and taken into account as they may directly impact the planning and designing of excavations and reinforcements in underground construction projects (Hoek and Brown, 1980; Hudson et al., 2011; Fransson et al., 2019; Fransson and Viola, 2021). Underground spent nuclear fuel repositories, for example,

require long-term tectonic stability and thus need to be built avoiding large brittle structures, since structural reactivation along a fault or a large fracture that intersects a spent nuclear fuel canister might jeopardize its integrity (e.g., Munier, 2006; McEwen et al., 2012). Therefore, the potential of (seismic) reactivation of pre-existing structures needs to be carefully assessed. Within the time period covered by the long-term safety assessment of a spent nuclear fuel repository, the formation and growth of new fractures has shown to be an improbable event and, as a consequence, the analysis of seismic risk is reduced to the analysis of pre-existing fractures and faults (SKB, 2011).

Major faults and fractures can be successfully modelled in 3D based on direct geological observations and can be avoided during the planning of the repository and positioning of the spent nuclear fuel canisters. Modelling, however, is commonly associated with inherent uncertainties, due to, for example, scarcity of data or poor conceptual understanding of the system under evaluation. Fortunately, the underlying geological uncertainties associated with complex deformation patterns may be significantly mitigated by constraining the geometry and kinematic history of the system under consideration through space and time. Hence, the study of geological properties and age relationships, particularly in the case of brittle deformation, becomes central to the understanding of the geological characteristics of a site.

The complex evolution and relative timing of multiple faulting and reactivation episodes in crystalline rocks can be unravelled through the detailed analysis of the structural geological record. Geometric, mechanical, metamorphic and kinematic considerations are used to understand complex fault architectures and fault rock assemblages as well as complex brittle relationships and histories (e.g., Viola et al., 2009; Scheiber and Viola, 2018; Tartaglia et al., 2020; Skyttä et al., 2021). The study of the fractal nature of brittle deformation is crucial because the

analysis of specific faults at any given scale of observation may provide insights into the development history and properties of fault systems at all scales. The geometry and kinematics of individual faults are important when aiming to group brittle features into internally coherent sets with similar properties (Angelier, 1994; Saintot et al., 2011; Mattila and Viola, 2014).

A major challenge when describing and unraveling the evolution of brittle structures in old, deeply exhumed basement rocks is the common lack of reliable time markers (such as sedimentary cover rocks or other well-dated geological objects) to help constrain in time deformation and correlate tectonic phases. This notwithstanding, the detailed evolution of some Precambrian faults and fracture networks has been successfully reconstructed by combining multidisciplinary studies integrating structural, geometric, kinematic and isotopic analyses (e.g., Mattila and Viola, 2014; Torgersen and Viola, 2014; Torgersen et al., 2015; Viola et al., 2016; Elminen et al., 2018; Scheiber and Viola, 2018; Uysal et al., 2020). While detailed structural analyses can help establish the relative age relationships of different brittle structures, isotopic dating methods can constrain the absolute age of deformation. The potassium-argon (K-Ar) geochronometer, for example, can be used to date synkinematic clays that form authigenically during faulting. In some cases, it has been possible to even date both the age of initial localization as well as of subsequent phases of structural reactivation (e.g., Dalrymple and Lanphere, 1969; Faure, 1987; Kralik et al., 1992; Haines and van der Pluijm, 2008; Viola et al., 2013; Viola et al., 2016; Scheiber et al., 2019; Tartaglia et al., 2020; Curzi et al., 2020a).

In this study, we use a combination of structural and geochronological investigations to unravel the brittle faulting and fault reactivation history at the ONKALO™ underground rock characterization facility and deep geological repository for spent nuclear fuel, currently
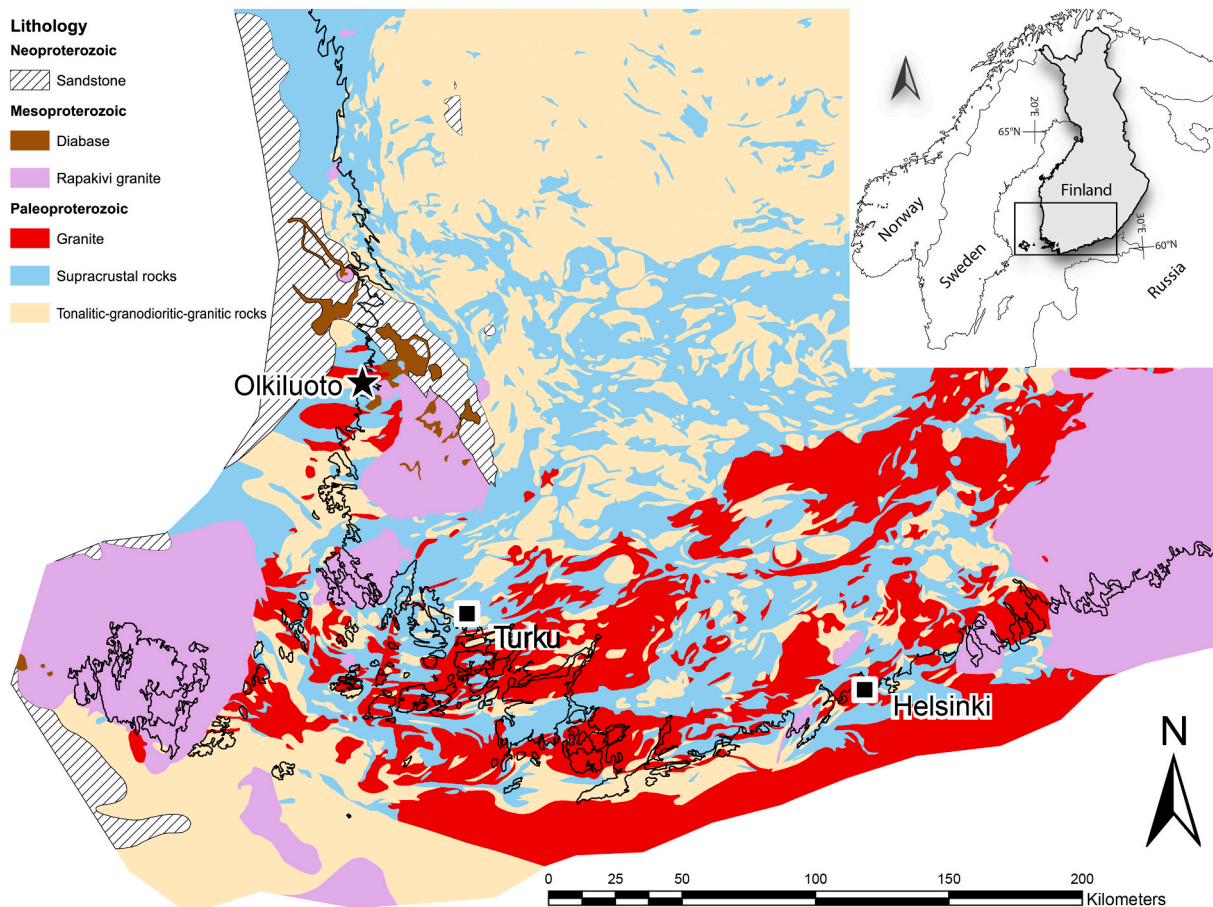

Fig. 1. Overview geological map of southwestern Finland. Olkiluoto Island is indicated by a black star.

under construction, on the island of Olkiluoto in southwestern Finland (Fig. 1). We collected an extensive dataset on brittle faults intersecting the ONKALO™ tunnels. We document the integrated multidisciplinary approach followed to characterize those brittle structures and to determine the relative age relationships of the occurring fault zones. To build an absolute time frame for the reconstructed faulting history, we also constrained the absolute timing of deformation by dating by K-Ar illite separated from fault gouge samples representative of specific fault sets. Based on this novel integrated and multidisciplinary analysis, we propose to classify brittle faults in ONKALO™ into four different fault systems, each characterized by internally consistent structural properties and tectonic histories. We suggest that our approach is of general validity and may integrate multidisciplinary studies aiming at reconstructing long and complex brittle histories of basement blocks (e.g., Scheiber and Viola, 2018), particularly during the siting process for repositories of spent nuclear fuel.

2. Geological setting of southwestern Finland

Olkiluoto is located within the central part of the Fennoscandian Shield, which was shaped during the Svecofennian orogeny (e.g., Gaál and Gorbatschev, 1987; Gorbatschev and Bogdanova, 1993; Nironen, 1997; Lahtinen et al., 2009; Bogdanova et al., 2015). The area consists of Paleoproterozoic supracrustal rocks and granitoids (Fig. 1). Peak deformation, metamorphism and magmatism during the Svecofennian orogeny occurred at 1.88–1.87 Ga (Nironen, 1997; Lahtinen et al., 2005). Shortening and significant crustal thickening were followed by crustal extension and orogenic collapse at 1.86–1.84 Ga, before a pulse of renewed compression caused by the collision of the Sarmatian Plate with the Fennoscandian Shield (Lahtinen et al., 2005). High temperature metamorphism between ca. 1.87 and 1.79 Ga caused anatectic melting and widespread migmatisation in the middle crust, accompanied by the emplacement of voluminous, late orogenic leucogranites (Ehlers et al., 1993; Kurhila et al., 2005; Kurhila et al., 2010). Lahtinen et al. (2005) proposed a second phase of orogenic collapse between 1.79 and 1.77 Ga.

The transition from an overall ductile to brittle deformation style for the rocks currently exposed in southwestern Finland occurred ca. 1.79–1.75 Ga ago (Torvela et al., 2008; Mattila and Viola, 2014). Although the geological events between 1.79 and 1.65 Ga are still quite poorly constrained, that time is nonetheless believed to have witnessed rapid cooling, high erosion rates, and exhumation of the now exposed bedrock from 10–15 km (Nironen, 2017) to 5–10 km depth by the Mesoproterozoic (Eklund and Shebanov, 1999; Heilimo, 2005).

The Paleoproterozoic rocks shown in Fig. 1 were intruded by anorogenic rapakivi granites and diabase dykes between 1.65 and 1.47 Ga (Rämö and Haapala, 2005; Rämö and Mänttäri, 2015). The Mesoproterozoic rapakivi magmas were sourced in the lower crust before a regional extensional/transtensional tectonic regime allowed them to intrude into upper crustal levels by exploiting existing brittle structures (Mattila and Viola, 2014). The 1.4–1.3 Ga Satakunta sandstone deposited in a WNW-ESE graben structure, which, most likely, formed in response to the same rifting event responsible for the emplacement of the rapakivi granites (Kohonen et al., 1993). The Satakunta sandstone is cut across by olivine diabase dykes and sills dated to 1.27–1.25 Ga (Suominen, 1991). Their emplacement likely relates to the early rifting phase of Laurentia and Baltica (Bingen et al., 2008). The current erosion level of the Finnish basement bedrock was established before the Cambrian (Kohonen and Rämö, 2005). Successions of Cambrian to Devonian sediments were subsequently deposited on top of this basement level (Larson et al., 1999; Van Balen and Heeremans, 1998) that was then stripped to become exposed again during Quaternary times.

2.1. Geology of the Olkiluoto Island

Olkiluoto is composed of Paleoproterozoic migmatitic supracrustal rocks, such as metapelites, meta-arenites and pyroclastic metavolcanites. Migmatites were intruded by two generations of pegmatitic granite at 1.86–1.82 Ga and 1.83–1.80 Ga (Mänttäri et al., 2010) and by Mesoproterozoic diabase dykes (Aaltonen et al., 2016) (Fig. 2). In addition, a porphyritic granite is found as either <2 m thick subhorizontal sills crosscutting the migmatitic foliation or as more irregular plutonic volumes. U-Pb dating of the porphyritic granite suite yielded a 1.8 Ga age (Mänttäri et al., 2007a; Mänttäri et al., 2010).

The ductile history of the Olkiluoto basement records four main deformation phases, referred to as D_{1-4} (Engström, 2013; Aaltonen et al., 2016). D_1 produced a weak schistosity locally overprinting a primary layering still preserved in the meta-supracrustal sequences. D_2 is the most important deformation phase as it affected the whole region, shaping the regional structural grain. Migmatisation during D_2 was widespread under amphibolite-facies metamorphic conditions (600–700 °C and 3.7–4.2 kbar) ca. 1.86–1.83 Ga ago (Tuisku and Kärki, 2010). D_2 structures encompass the regional pervasive ~E-W to NE-SW gneissic foliation in addition to NE-SW striking folds and shear zones. During D_3, the strongly migmatised and foliated bedrock was deformed in a heterogeneous fashion, as shown by F_3 folds with SE dipping axial planes or dextral, E-W striking, high-grade shear zones. D_4 formed NNE-SSW folds generating complex interference patterns with the older folds and ductile shear zones generally parallel to the axial surfaces and/or fold limbs.

Hornblende, biotite, and muscovite $^{40}Ar-^{39}Ar$ dating from Olkiluoto (Aaltonen et al., 2016) constrains the transition from the ductile to the brittle regime to ca. 1.79–1.72 Ga. In addition, it shows that the 1.57–1.55 Ga old rapakivi granite intrusions near Olkiluoto (Vaasjoki, 1996; Rämö and Haapala, 2005) cooled down to below 300 °C during a 10–20 Ma long time period without causing any significant regional thermal overprint. The brittle structural history of the area was steered by the inherited ductile structural grain (Mattila and Viola, 2014; Skyttä and Torvela, 2018). Microstructural and fluid inclusion studies from Olkiluoto have revealed that the first brittle structures formed already within the brittle-ductile transition zone, in response to transient and cyclical fluctuations of the fluid pressure (Marchesini et al., 2019; Prando et al., 2019). Paleostress inversion analysis fault-slip data has led to the recognition of at least seven distinct brittle deformation stages (Mattila and Viola, 2014, their Fig. 18 and 19). According to Mattila and Viola (2014), the Svecofennian Shield became "saturated" with brittle structures (meaning that no new brittle structures formed since then) already during the Mesoproterozoic. Hence, all fault systems from Olkiluoto are interpreted as having nucleated between ca. 1.75 Ga and 1.0 Ga. In the Neoproterozoic, renewed deformation took place in the form of reactivation, while no new faults nucleated.

In general, faults in Olkiluoto are mainly i) low-angle faults dipping gently to moderately towards the SE, ii) E-W striking faults dipping gently to moderately to the SSE-SSW and iii) subvertical to vertical faults striking on average N-S or NNW-SSE (Aaltonen et al., 2016; Mattila and Viola, 2014). Crosscutting relationships between major fault zones can be rarely observed in Olkiluoto, due to, the tunnel layout being specifically designed to avoid such intersections.

3. Structural data and methods

3.1. Hierarchical classification of faults

To effectively describe the Olkiluoto brittle structural framework and to produce a hierarchical classification of faults and their sorting into internally consistent groups, we rely here on the conceptual classification proposed by Nordbäck and Mattila (2018). They proposed to classify faults and fault sets as follows: **Fault**: single fault plane or shear fracture; **Fault zone**: network of interconnected faults, fault strands and fractures with a well-defined fault core (or cores) and damage zone, which can be taken as forming a single tabular geological object; **Fault system**: cluster of more than one fault zone; **Fault complex**: cluster of more than one fault system.
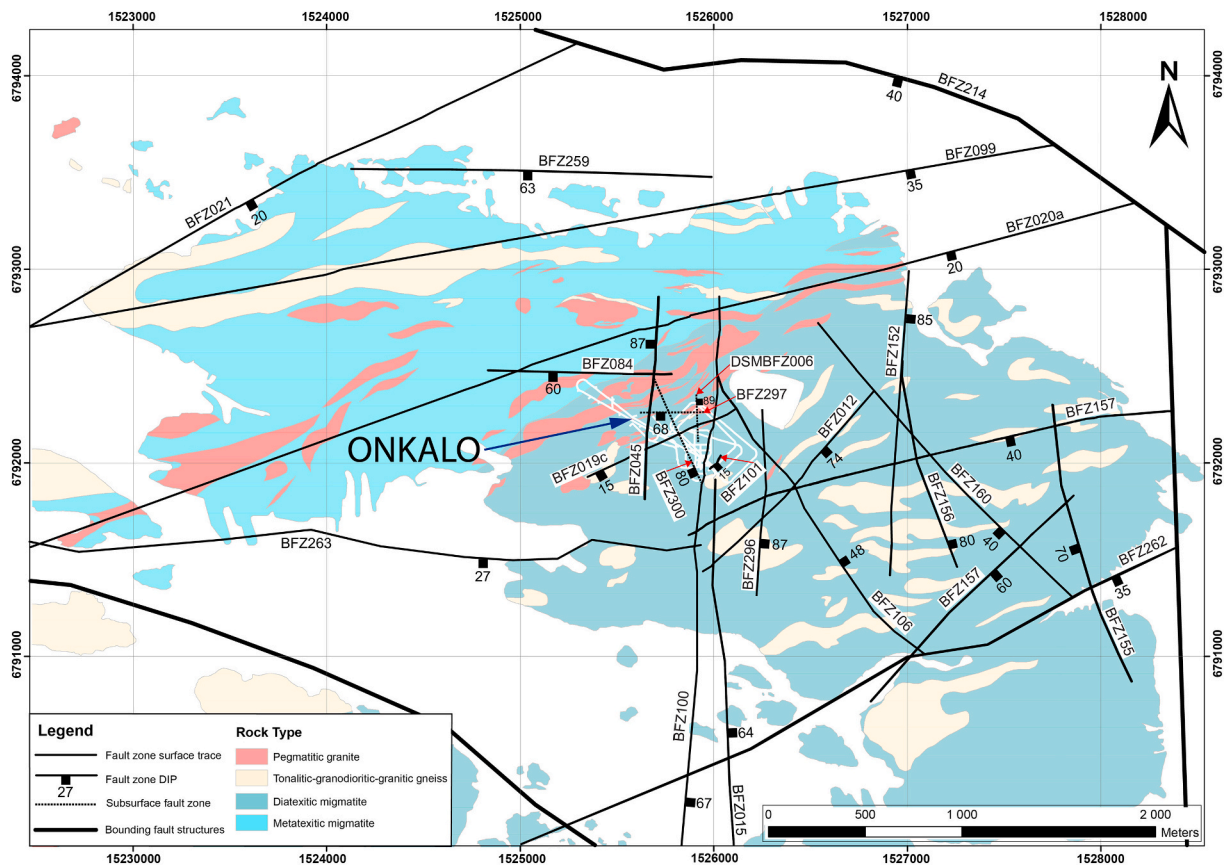
Fig. 2. Geological map of Olkiluoto Island, visualising fault zones of this study and other high to medium confidence fault zones from Aaltonen et al. (2016). The location of ONKALO™ is indicated by the blue arrow and tunnel white layout. Modified after Aaltonen et al. (2016). (For interpretation of the references to colour in this figure legend, the reader is referred to the web version of this article.)

In this study, the smallest considered structural unit corresponds to mesoscopic single-plane faults with a documented length in the meter to tens of meter range (Nordbäck, 2014). Also, we consider a fault system to be composed of multiple fault zones formed during the same tectonic event and with a mechanically compatible orientation in addition to a similar fault rock assemblage and kinematics. A fault system can be defined at a scale from hundreds of meters to kilometres. The grouping of fault zones into fault systems builds upon the work by Nordbäck and Mattila (2018), and is further strengthened by additional data and results presented in this study. A fault complex encompasses all the fault systems from an investigated area or rock volume. A fault complex may thus be composed of fault systems of different age, kinematics and orientation.

3.2. Underground mapping data

A total of eleven fault zones were investigated in this study (Fig. 3), each considered to be representative of some key geological characteristics such as fault rock type and orientation and kinematics of the different fault systems from ONKALO™. In addition to these fault zones, some other minor fault structures were also investigated and used to constrain specific crosscutting relationships between the structures of the different fault systems.

ONKALO™ contains a 5 km long access tunnel, numerous shorter tunnels and three shafts reaching 455 m from the ground surface (Fig. 4A). In this study we have used the geological mapping dataset collected during the construction of ONKALO™ between 2004 and 2018. As part of the tunnel mapping procedures, the location and properties of all lithological and structural elements were described, including geometrical and topological information on all fractures with

trace length > 0.25 m (Nordbäck and Engström, 2016). This exceptionally large fracture trace dataset contains information on geometry and topology of over fifty thousand mapped fractures (Fig. 4A). Geological parameters have been systematically collected and 3D trace maps have been generated for all mapped faults and fractures (Fig. 4A). For shear fractures, information on slip direction and sense of movement is available as observed on slickensided surfaces (Fig. 4B). The exact location, geometry and dimension of fault zones intersecting the tunnel have been determined and are reported separately for damage and core zones of each fault. The width of damage zones is defined as the thickness of the rock volume (enveloping a fault core) wherein fracture intensity is higher than background values or where secondary fault structures such as Riedel fractures, are found around the core.

In this study we integrated the database by Nordbäck and Mattila (2018) with additional structural mappings from all accessible tunnel and shaft sections, the analysis of photographs systematically taken from along the tunnel walls and structural interpretations based on digitised and measured fracture trace data. We use fault trace data to confirm the extent of damage zones for some of the larger fault zones (Fig. 4C). By interpreting the trace data from secondary fault structures (e.g., Riedel and step-over fractures), we were also able to define the kinematics of some of the fault zones (Fig. 4D). For information on the length of faults and fault zones we relied on results from the 3D modelling by Aaltonen et al. (2016). Detailed tunnel photography (Fig. 5A) enabled us to define the hosting lithology, the presence of possible ductile precursors and other geometrical parameters of fault zones. As part of our additional structural mapping, we used drone photography to document outcrops where faults were exposed in the tunnel floor (Fig. 5B).
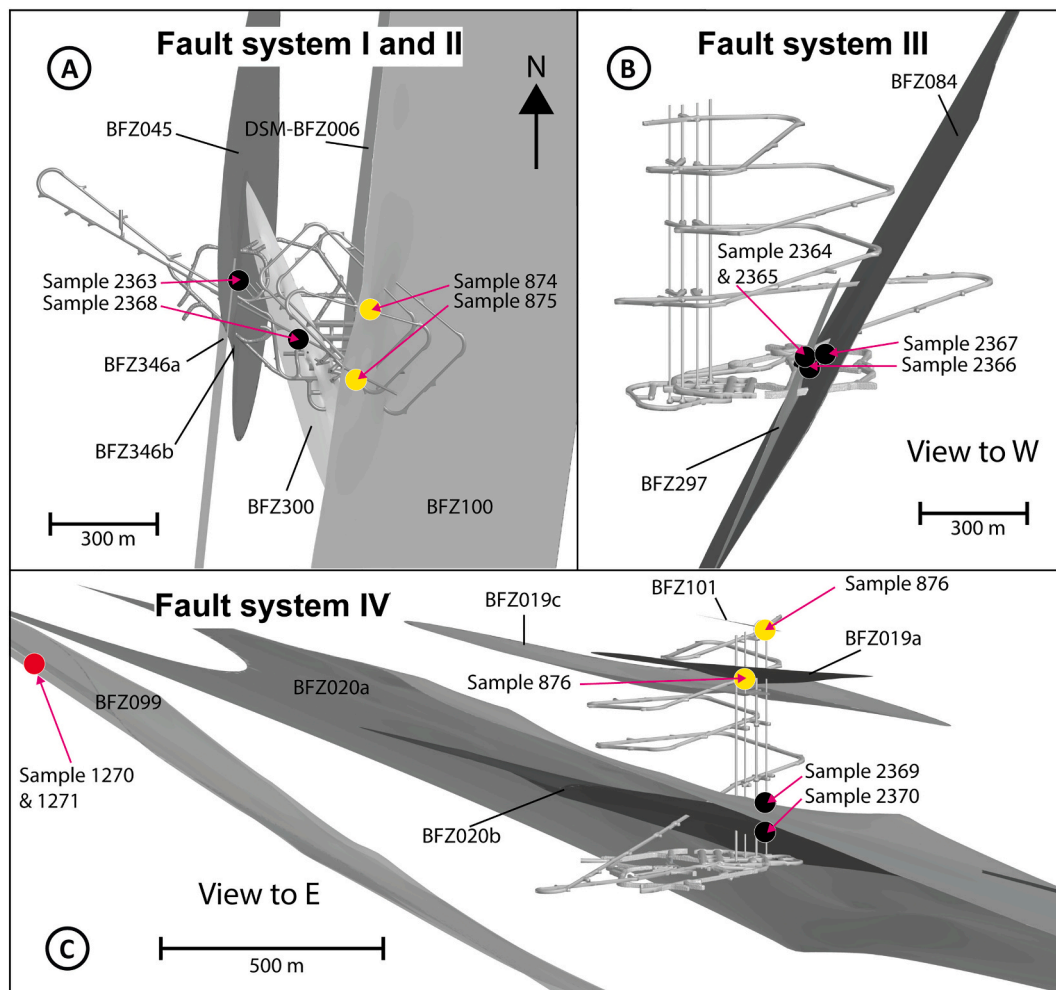
Fig. 3. A) Bird's eye view of 3D models of the studied N-S (Fault system I) and NNW-SSE (Fault system II) striking sub-vertical fault zones and associated K-Ar fault gouge samples. B) Image displaying the 3D models of the studied *E*-W (Fault system III) striking fault zones and associated K-Ar fault gouge samples, view towards west. C) Image displaying the 3D models of investigated low-angle (Fault system IV) fault zones and associated K-Ar fault gouge samples, view towards east. In all figures the K-Ar samples of this study are shown as black dots, samples by Mänttäri et al. (2007b) in yellow and samples by Viola et al. (2011b) in red. K-Ar fault gouge sampling procedures and the dating methodology are detailed in the text. (For interpretation of the references to colour in this figure legend, the reader is referred to the web version of this article.)

4. Description and classification of fault zones

The investigated faults and fault zones have been classified into four different systems based on distinctive features, such as orientation, kinematics, fault rocks and fracture filling mineralogy. We name the different fault systems Fault systems I- to IV (Table 1) and describe their characteristics in the following chapters.

### 4.1. Structural characteristics of the main fault systems

4.1.1. Fault system I

Faults of Fault system I on average are sub-vertical (84°) and strike NNE-SSW (008°), are sinistral strike-slip (Fig. 3A), and cut discordantly the regional foliation. The average slip direction plunges 10° towards 005° (Fig. 6A). Along single-plane faults we mapped apparent displacements in the order of a few centimetres, whereas for fault zones the apparent cumulative displacements may reach up to 2 m (Pere, 2009). The modelled lengths of the fault zones in this fault system reaches ca. 4 km (Aaltonen et al., 2016).

Mylonitic fault rocks are a unique feature of the Fault system I fault cores (Fig. 6B&C), as mylonites have not been observed in any of the other fault systems. Fault system I cores contain quartz veins as well as

breccia layers and pockets with quartz, chlorite, sphalerite, pyrite, chalcopyrite and galena. Mylonites are invariably reworked, and thus postdated by the breccias. Two generations of 1–20 cm thick quartz veins have been reported to typically occur within the core of these fault zones (Prando et al., 2019). The veins are described as being hydrothermal in origin and are usually associated with sulphides, epidote, as well as clay smearing along discrete slip surfaces that formed along the vein-host rock interface. The quartz veins are in turn crosscut by calcite-filled fractures.

The thickness of the fault cores for System I is between 0.1 and 0.5 m for faults that are less than 1 km in length and between 0.1 and 2 m for faults longer than 1 km. A 1–2 m thick and hydrothermally altered zone is usually associated with the core of the larger structures. Damage zones contain variably oriented secondary fractures and Riedel shears. The maximum width of the damage zones may reach up to 20 m. The kinematics of Fault system I structures is sinistral strike-slip, as documented by synthetic R and antithetic R' fractures (Fig. 6C) and slickensided planes, although a few dextral faults are also present (Fig. 6A) forming similar dihedral angles to the fault zones as the sinistral R fractures (Fig. 8A & B).
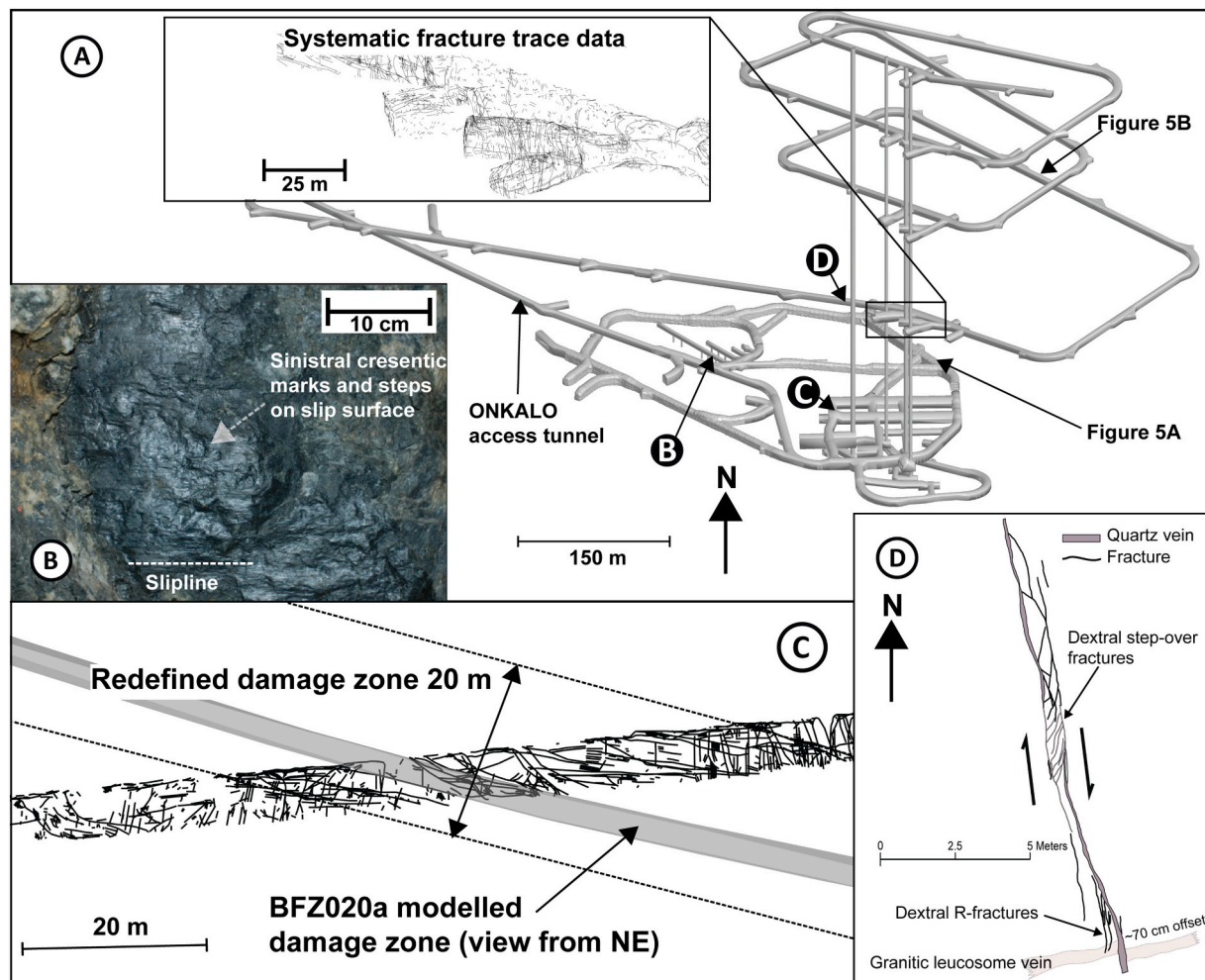
Fig. 4. Examples of different tunnel mapping datasets from ONKALO™. A) 3D image of the ONKALO™ access tunnel with an example of the systematic fracture trace data (inset). The location of Figs. 3B, C, D, 5A and B is shown by labelled arrows. B) Sinistral slickenside fault plane (BFZ045) in demonstration tunnel 2, width of image is approximately 40 cm. C) Example of how the detailed fracture trace data were used to refine the width of the damage zone for brittle fracture zone BFZ020a. D) Example of how the kinematics of brittle fracture zones could be at times constrained by mapping, studying and interpreting the associated secondary fracture patterns extracted from the fracture trace data. The figure depicts brittle fault zone BFZ300 (see Marchesini et al., 2019) with dextral step-over fractures and a set of mesoscopic dextral Riedel fractures.

4.1.2. Fault system II

Fault system II is composed of sub-vertical, NNW-SSE striking (340°) and steeply SW dipping (80°) dextral fault zones (Fig. 3A) that lack ductile precursors and cut through the structural grain of the migmatitic gneiss. The average slip direction plunges 07° towards 346° (Fig. 6D).

Fault system II fault zones have cores containing at least one relatively thick quartz vein, which may branch into multiple segments with connecting dextral step-over structures (Fig. 6E & F). Two different quartz generations have been recognised as forming the veins, with one pervasively dynamically recrystallised quartz generation postdated by a generation of white and more pristine quartz (Marchesini et al., 2019). Quartz veins containing chlorite, calcite and sulphides occur in the second generation (Marchesini et al., 2022). The thickness of the veins varies between 20 cm in the core of the kilometre-long fault zones and a few millimetres in the smaller ones. The damage zones contain Riedel fractures that are geometrically compatible with dextral strike-slip faulting (Fig. 6E), and long fractures parallel to the fault cores. Some localised evidence of sinistral strike-slip faulting has also been registered from the southernmost intersections of BFZ300 in ONKALO™. The width of the damage zone is 4–12 m for structures ≥1 km and up to a couple of meters for fault zones up to 100–200 m in length. An up to 2 m thick alteration zone also usually envelopes the core of the fault zones.

Due to their similar orientation, small dextral Fault system II shear structures are difficult to distinguish from Fault system I Riedel fractures (Fig. 8A & B). From the 3D modelling of Fault system I and II fault zones, a fault zone pattern emerges where Fault system II fault zones (Fig. 8C & D) abut against fault zones belonging to Fault system I (Fig. 9F), thus suggesting that Fault system II is either coeval or postdating Fault system I (Peacock et al., 2017).

4.1.3. Fault system III

Fault system III comprises E−W striking (092°), sub-vertical to moderately south-dipping (64°) fault zones (Figs. 3B; 7A). Slip is mainly oblique dextral with an average slip direction plunging 35° towards 252° (Fig. 7A), although sinistral reactivation has probably occurred as suggested by a few fault planes displaying a sinistral or reverse sense of movement. These mainly follow and exploit ductile precursors consisting of E−W trending and moderately south-dipping dextral D_3 ductile shear zones (Fig. 8E). Up to 1 m apparent displacements have been measured for the fault zones of Fault system III. The ductile structures acting as precursors to Fault system III are composed of meter scale sheared tabular volumes containing a pervasive foliation (Fig. 7B). Local variations in the orientation of the ductile shear zones affect the orientation and localisation of the Fault system III structures. At some
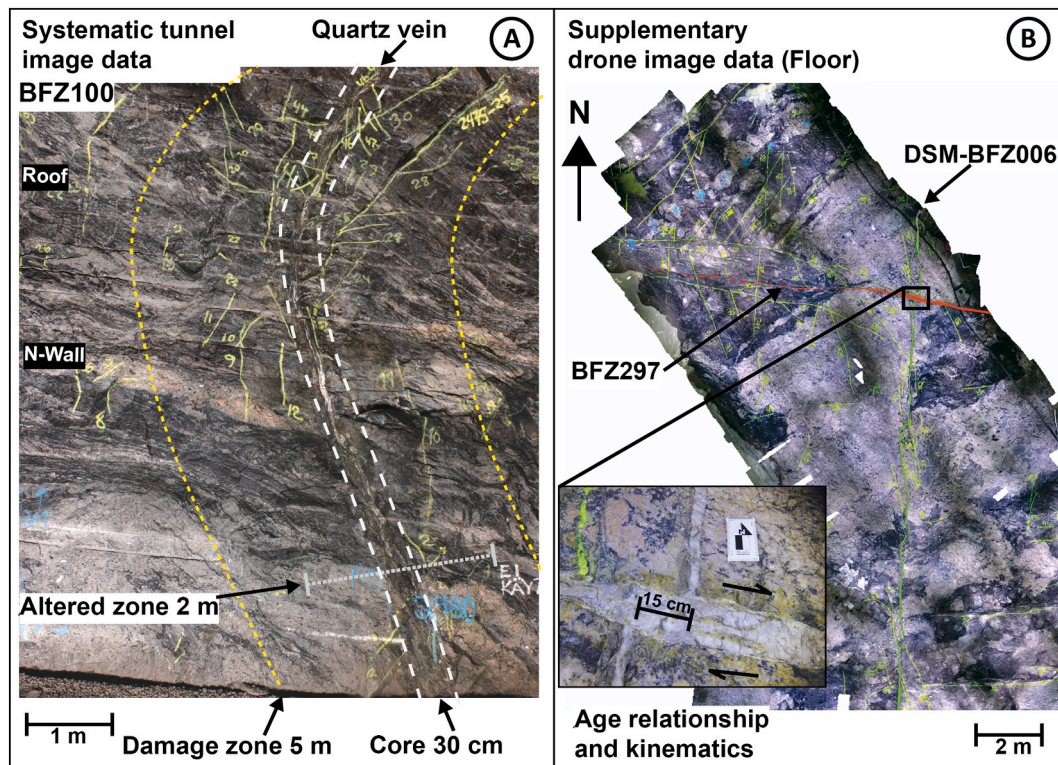
Fig. 5. A) Tunnel photograph, used for characterising the internal structure of brittle fracture zone BFZ100 from structures observed in a wall and parts of the roof of the ONKALO™ access tunnel, chainage 2475–2480 m. B) A supplementary drone orthomosaic image from the floor of the Vehicle Access Tunnel 1, acquired as part of this study. Crosscutting relationships between BFZ297 and DSM-BFZ006 are observed in the floor. The locations of Fig. 5A and B are pointed out with arrows in Fig. 4A. The faint yellow lines on tunnel walls are paint marks from tunnel mapping. (For interpretation of the references to colour in this figure legend, the reader is referred to the web version of this article.)

Table 1
Fault zones assigned to the four fault systems.

Faults system	Orientation	Kinematics and geological features	Fault zones (11)	K-Ar samples (8)
Fault system I	N-S striking, sub-vertical	Sinistral, mylonitic fault rock, breccia, hydrothermal quartz veins and gouge	BFZ045, BFZ100, BFZ346a	2363 (BFZ045)
Fault system II	NNW-SSE striking, sub-vertical	Dextral, two generations of hydrothermal quartz veins	BFZ300, BFZ346b, DSM-BFZ006	2368 (BFZ300)
Fault system III	E-W striking, steeply S-dipping	Oblique dextral, ductile precursor, breccia, hydrothermal quartz veins, gouge and clay	BFZ084, BFZ297	2364 (BFZ297) 2365 (BFZ297) 2366 (BFZ297) 2367 (BFZ084)
Fault system IV	Low-angle, gently SE-dipping	Reverse, ductile and lithological precursor, crushed rock, gouge and clay	BFZ019c, BFZ020a, BFZ020b	2369 (BFZ020a) 2370 (BFZ020b)

locations, fault zones have been observed to also exploit *E*-W striking contacts between different lithologies although at times they also crosscut the foliation of the moderately foliated migmatite gneiss they cut across (e.g., brittle fault zone BFZ297 in Fig. 7C).

The cores of the <1 km long Fault system III fault zones are tens of centimetres thick and consist of quartz cemented breccia, gouge and clay. Dextral Riedel fractures and rocks altered by chloritisation, sulphiditisation and graphitisation are the main features of Fault system III damage zones, which may be up to 10 m in thickness but generally are only a couple of m thick. In the Vehicle Access Tunnel 1 (Fig. 5B), an up to 1 cm thick illite layer was observed at the edges of the BFZ297 core.
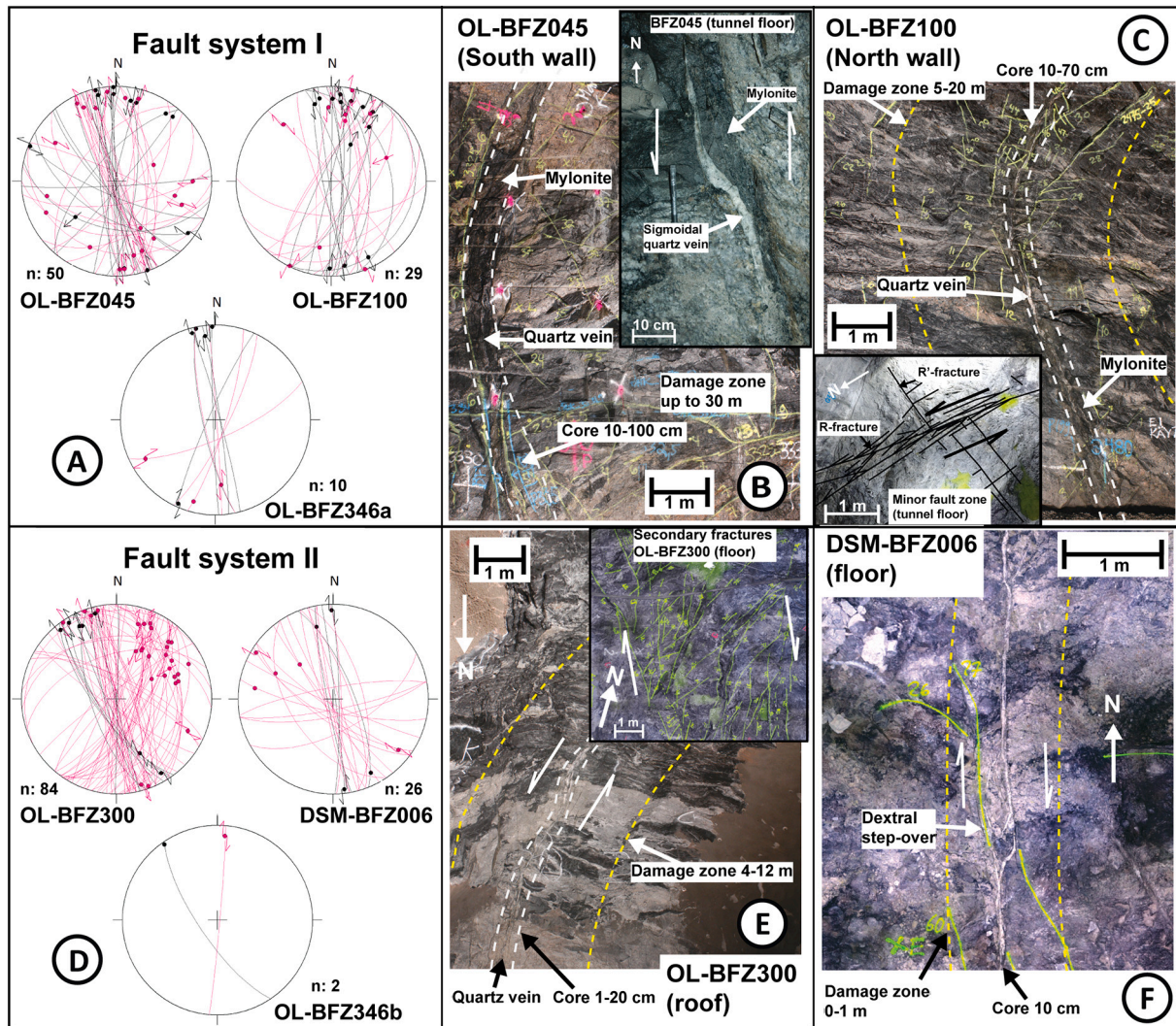
4.1.4. Fault system IV

Fault zones of Fault system IV dip on average gently to the SE (dip/dip direction 18/143°, Figs. 3C and 7D), although their orientation can locally be quite irregular. Mainly based on data from the structural logging of drill cores, the kinematics of Fault system IV slickensided surfaces are mostly indicative of reverse faulting, although normal slip is locally also present. At the tunnel scale however, the sense of movement of Fault system IV is unfortunately not always clear (Fig. 7D). The gentle dip of Fault system IV structures allows for longer intersections with the tunnel walls compared to any of the other structures, which, as discussed, are much steeper fault systems. Mapping indicates displacements in the order of a few tens of centimetres for the <100 m long BFZ101 fault zone; the displacement magnitude and kinematics of some of the longer (> km) fault zones is still poorly constrained.

The position of Fault system IV structures is partly controlled by ductile shear zones assigned by Aaltonen et al. (2016) to D_4 and the occurrence of porphyritic granites (Fig. 7E). The porphyritic granites occur in the ONKALO™ tunnel as either irregular bodies or as narrow 0.5–2 m thick sub-horizontal sheets that usually cut the migmatitic regional foliation at a small angle. Although the contacts between migmatites and porphyritic granites seem to be the most important planes of mechanical weakness, and thus the key anisotropy to localise

Fig. 6. Kinematic fault data (lower-hemisphere Schmidt projection) from the investigated fault zones (black great circles: fault cores, pink great circles: fault damage zone) and photographs from selected fault zones of Fault systems I and II. Lines and arrows in the photographs indicate different parts of the fault zones (core zone, damage zone etc.) and sense of movement. The faint yellow lines on tunnel walls are paint marks from tunnel mapping. The bend between tunnel wall and roof causes a curved appearance of the fault zones. The orientation of the photographed tunnel face is indicated under the fault zone name and as north arrows for roof and floor photographs. The fault zones are grouped by the fault system approach highlighted and discussed in the paper. (For interpretation of the references to colour in this figure legend, the reader is referred to the web version of this article.)

later brittle deformation, Fault system IV structures are also partly controlled by the foliation of the migmatitic basement rocks. Where the foliation thereof is pervasive or where porphyritic granites are not present, the Fault system IV structures exploit the pre-existing weakness planes formed by the foliation of migmatites. As a result of the influence of the gently dipping porphyritic granites, Fault system IV structures display a somewhat lower dip angle than the general foliation dip of the migmatites (Fig. 8F). Depending on the direction of the porphyritic granites, Fault system IV fault zones may locally be N- or W-dipping and due to this strongly undulating behaviour may locally appear as a NW dipping normal faults, although the fault planes actually represent SE dipping thrusts when interpreted at the larger scale. Nevertheless, kinematic indicators suggesting localised extension are also present within the fault slip database.

The core of the Fault system IV fault zones contains lenses and pockets of crushed rock, gouge and clay (Fig. 7F), which can be up to a couple of m but, normally, are only a few cm thick. These fault products are compatible with the <100 °C hydrothermal fracture filling assemblages described by Aaltonen et al. (2018). Their damage zones, which may be up to 10 m thick, are characterized by zone-parallel fractures

coated by chlorite, calcite, pyrite and various types of clays as filling. The thickness of the damage zones is usually lower where the fault zones follow the contacts to the porphyritic granites compared to areas where porphyritic granites do not occur (Fig. 7E & F).

4.2. Relative age relationships between fault systems

Crosscutting relationships between the studied fault zones are only sporadically observed in the excavated tunnels, such that the systematic analysis of the relative timing of deformation is difficult. Crosscutting relationships are, instead, more commonly observed for the smaller faults (single plane faults) or between fault zones and single plane faults. These were thus studied making it possible to conclude the following: Fault system I and II single plane faults are systematically cut across and offset by fault zones belonging to Fault system III (Fig. 9A–D) and Fault system IV (Fig. 9E). In addition, based on indirect (3D modelling) and direct outcrop observations, we conclude that Fault system II fault zones abut against the Fault system I fault zones (Fig. 9F),which indicates that Fault system II is either kinematically linked to or postdates Fault system I (Peacock et al., 2017). We note that small single plane faults do not
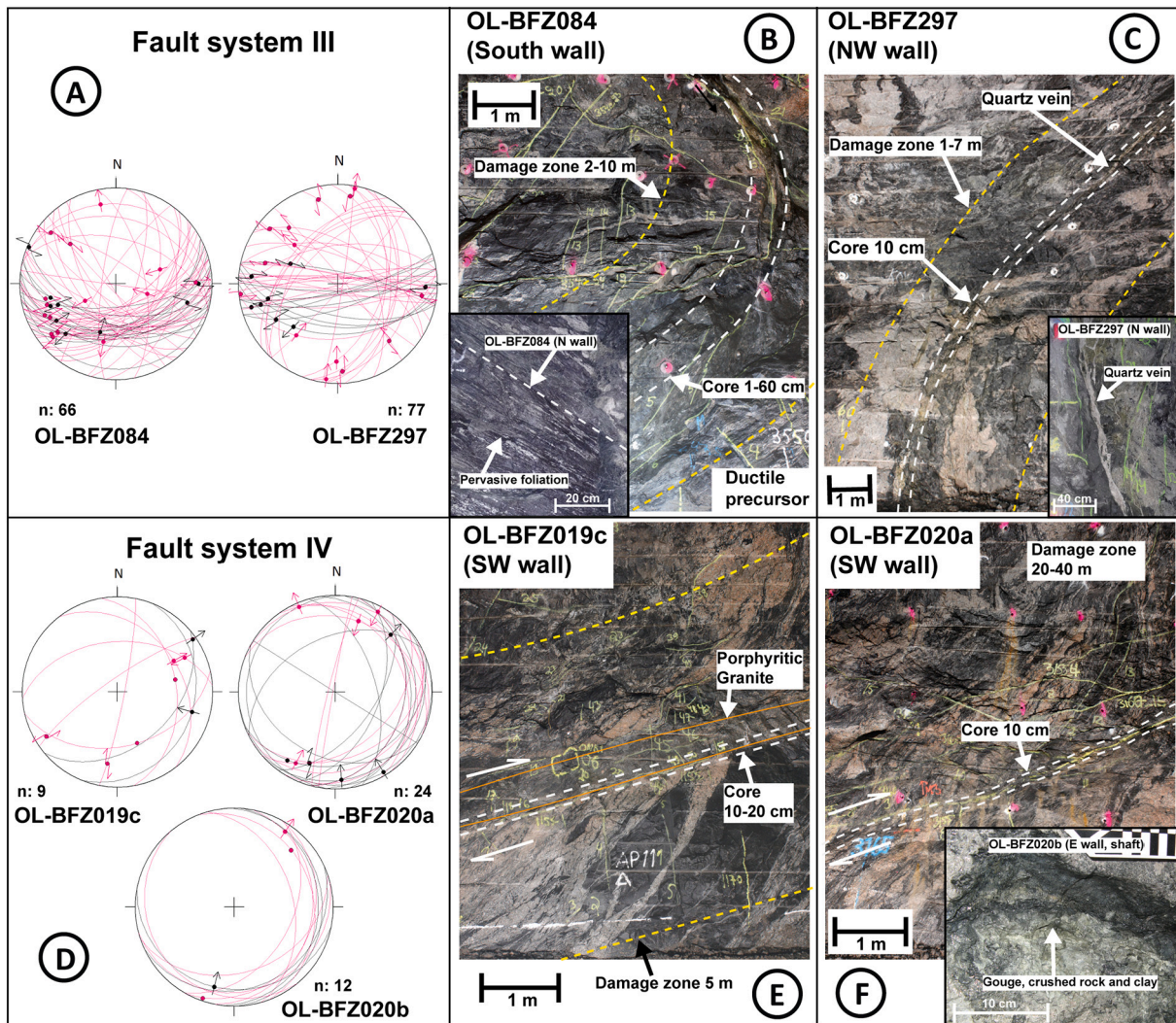
Fig. 7. Kinematic fault data (lower-hemisphere Schmidt projection) from the investigated fault zones (black great circles: fault cores, pink great circles: fault damage zone) and photographs from selected fault zones of Fault systems III and IV. Lines and arrows in the photographs indicate different parts of the fault zones (core zone, damage zone etc.) and sense of movement. The faint yellow lines on tunnel walls are paint marks from tunnel mapping. The bend between tunnel wall and roof causes a curved appearance of the fault zones. The orientation of the photographed tunnel face is indicated under the fault zone name. The fault zones are grouped by the fault system approach highlighted and discussed in the paper. (For interpretation of the references to colour in this figure legend, the reader is referred to the web version of this article.)

necessarily invariably record the full deformation history typical of the larger fault systems they belong to, as reactivation may have been highly heterogeneous and selective.

At the intersection between structures DSM-BFZ006 (Fault system II) and BFZ297 (Fault system III; Fig. 9A), a much more pronounced epidotization and illitisation front affects the surrounding host rock in BFZ297 than in DSM-BFZ006. Cross-cutting relationships between Fault system III structures and Fault system IV structures have not been observed but the lack of quartz and hydrothermal alteration within Fault system IV may suggest that it formed at a later stage than the first three fault systems, which all contain quartz veins and hydrothermal alterations. Based on the observed relative age relationships, the proposed relative chronology of the identified fault systems is, from oldest to youngest, Fault system I to IV.

5. K-Ar fault rock dating

5.1. K-Ar dating technique

The analytical approach used to date illite from the sampled fault gouges was described in detail in Zwingmann and Mancktelow (2004), while a more recent general description of the procedure can be found in Viola et al. (2018). Additional information can be found in Appendix A. Seven standards (3 HD-B1, 3 LP6 and 1 GLO (Odin and 35 collaborators, 1982; Hess and Lippolt, 1994)) and four airshots (small aliquots of air) were analysed (Table 2). The error for the $^{40}Ar/^{36}Ar$ value of the airshots yielded 295.98 ± 0.33 (1 sigma). The general error for the age standard is below 1% (1 sigma). K-Ar ages were calculated by using the ^{40}K abundance and decay constants recommended by Steiger and Jäger (1977). The age uncertainties consider the errors during sample weighing, $^{38}Ar/^{36}Ar$ and $^{40}Ar/^{38}Ar$ measurements and K analysis. K-Ar
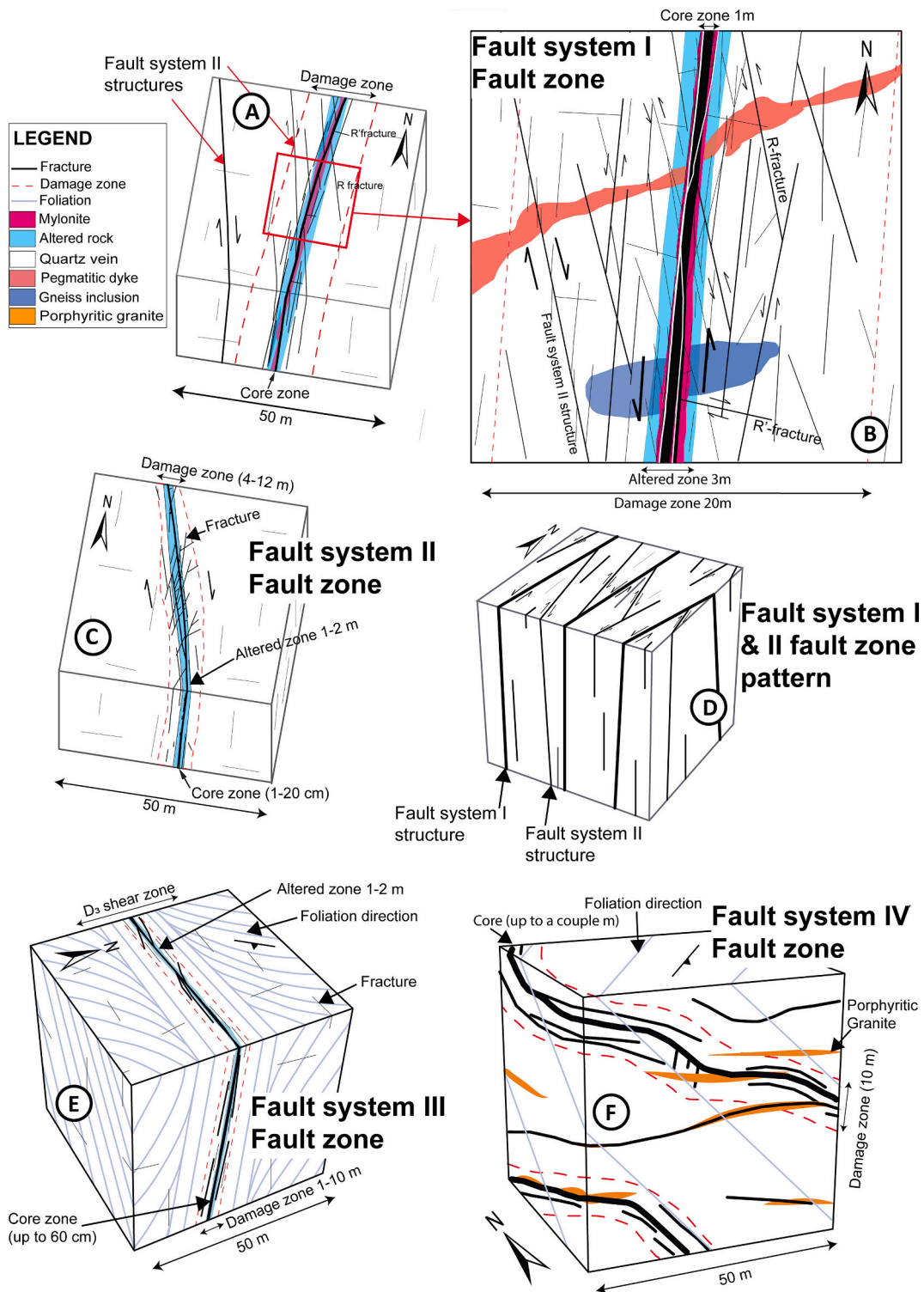
Fig. 8. Schematic 3D block diagrams of idealised representative fault zones of the four identified Fault systems at 50 m scale. A) Illustration of a Fault system I fault zone. B) Illustration of the internal structure of a typical Fault system I fault zone (note the 20 m scale bar). C) Characteristics of a Fault system II fault zone. D) Schematic illustration of the Fault systems I and II fault zone pattern. E) Illustration of a Fault system III fault zone. F) Illustration of a Fault system IV fault zone.

age errors are reported within 1 sigma uncertainty.

5.2. K-Ar samples and preparation

Eight representative fault rock samples (Fig. 5) of approximately 80 to 500 g each were collected from the ONKALO™ tunnel from the core of six different fault zones. One sample was collected from Fault system I,

one sample from Fault system II, four samples from Fault system III and two samples from Fault system IV. The samples are from depths between −337 m to −437 m from ground surface. A total of 33 clay fractions were separated from the samples and analysed by K-Ar.

To enable validation of the geochronological results, the dated sample material must be characterized by a wide range of analytical techniques including: X-ray diffraction (XRD), scanning electron
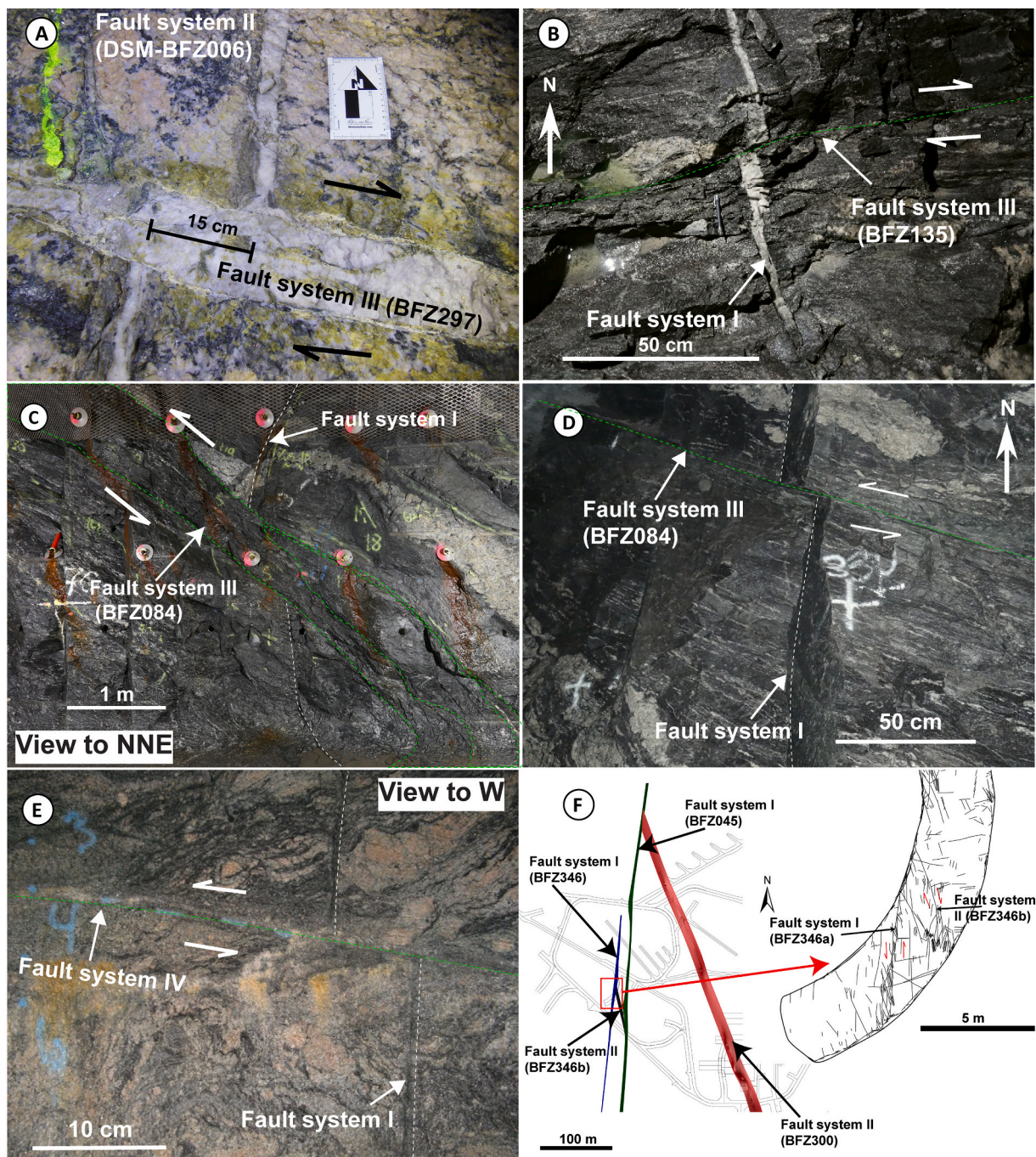
Fig. 9. Examples of crosscutting relationships between fault zones, faults and fractures from ONKALO™. A) Fault system III fault zone BFZ297 crosscutting and offsetting Fault system II fault zone DSM-BFZ006 in the floor of vehicle access tunnel 1. B) Fault system III fault zone BFZ135 crosscutting and offsetting a Fault system I fault in the floor of vehicle access tunnel 11. C) Fault system III fault zone BFZ084 crosscutting and offsetting a quartz-filled Fault system I fault in the wall of demonstration tunnel 2, view towards the NNE (modified after Aaltonen et al., 2016). D) Fault system III fault zone BFZ084 crosscutting and offsetting Fault system I fractures in the wall of vehicle access tunnel 15. E) Fault system IV fault crosscutting and offsetting a Fault system I fault in the personnel shaft −14 m level, view towards W. F) Horizontal cross-section (−400 m level) of 3D models representing the NNW-SSE striking sub-vertical Fault system II fault zones BFZ346b, BFZ300 and N-S striking sub-vertical BFZ045 and BFZ346a Fault system I fault zones. The Fault system II fault zones are modelled as joining the Fault system I fault zones. BFZ346b fault zone is well constrained by the tunnels and the abutting relationship to BFZ346a is visible in the floor (zoomed in on the right image) of ONKALO™ (Tunnel id: tt-4366).

microscopy (SEM) and particle granulometry (see summaries in Vrolijk et al., 2018; Viola et al., 2018; Curzi et al., 2020a; Tsukamoto et al., 2020). For this study, grain size fractions <2 μm in size were separated in distilled water according to Stoke's law. Additional sub-μm grain size fractions of <0.1 and 0.4 μm were obtained using a large capacity high speed centrifuge.

Freshly broken surfaces of gouge sample chips were carbon coated and examined by SEM using a Zeiss EVO equipped with an energy dispersive system X-ray analyzer (EDS) (Fig. 11A). The mineralogy of the size fractions was determined by XRD on air-dried and glycolated samples following the approach outlined in Moore and Reynolds (1997). XRD analytical procedures are described further in Appendix A.

Table 2
K-Ar age standard and airshot data.

CSIRO ID	K	Rad. ^{40}Ar	Rad. ^{40}Ar	Age	Error	Error to reference
Standard	[%]	[mol/g]	[%]	[Ma]	[Ma]	[%]
HD-B1–125	7.96	3.3574E-10	92.0	24.17	0.36	−0.17%
HD-B1–127	7.96	3.3187E-10	88.8	23.89	0.36	−1.32%
HD-B1–128	7.96	3.3840E-10	91.9	24.36	0.37	0.62%
LP6–139	8.37	1.9370E-09	97.3	128.72	1.88	0.64%
LP6–141	8.37	1.9236E-09	97.0	127.86	1.88	−0.03%
LP6–142	8.37	1.9162E-09	97.4	127.39	1.88	−0.40%
GLO-164	6.55	1.1199E-09	92.9	95.97	1.53	0.99%

Airshot data		
ID	^{40}Ar/^{36}Ar	+/−
AS121-AirS-1	296.96	0.24
AS123-AirS-1	295.40	0.23
AS124-AirS-1	294.92	0.42
AS126-AirS-1	296.63	0.45

K-Ar standards.

## 6. Sample characterization and age determination

6.1. Mineralogy of clay samples

The mineralogical composition of the dated grain-size fractions was determined by X-ray diffraction (XRD; Fig. 10; Appendix B). The analysed gouges exhibit a significant variability in mineralogy and proportions of the occurring minerals, whereas different size fractions from the same gouge samples are, instead, mineralogically quite similar. The most common clay minerals are smectite, chlorite and illite. Most samples contain the 2M$_1$ illite polytype but sample 2370 also contains 1M/1M$_d$ (lower temperature) illite and small amounts of chlorite. The illite/mica 2M$_1$ polytype can represent a mixture of authigenic and detrital illite/mica (protolithic muscovite). However, since the bedrock in Olkiluoto contains less than 4% muscovite (Kärki and Paulamäki, 2006), we exclude significant protolithic muscovite contamination (Zwingmann et al., 2010; Viola et al., 2013). SEM imaging of the sample material (Fig. 11A), documents the systematic presence of idiomorphic illite with regular, euhedral grain boundaries with sharp edges, typical for an authigenic and synkinematic origin in gouge samples from Fault system I and IV. SEM investigation of samples collected from Fault system II and III, on the other hand, seems to suggest a lesser extent of deformation, as indicated by typical illite/smectite aggregates.

6.2. K-Ar illite age results

K-Ar illite ages were obtained from the separated <0.1 to 6–10 μm clay-size fractions (Table 3), with radiogenic ^{40}Ar content ranges from 90.1 to 99.7% indicating reliable analytical conditions for all analyses. K concentrations range from 2.3 to 6.5% as function of the heterogeneous mineralogy of the dated fractions. The ages vary between 916.3 ± 18.6 Ma to 1549.7 ± 31.7 Ma. A clear trend of decreasing age with decreasing grain size is documented (Figs. 11B and 12), with age differences between the coarsest and the finest fractions from the same sample between 147.4 and 384.6 Ma. K-Ar ages from Fault System I range between 1275.9 ± 26.4 Ma and 1549.7 ± 31.7 Ma (1 sample, 4 fractions). For fault system II, ages range between 1102.4 ± 23.4 Ma and 1400.5 ± 29.2 Ma (1 sample, 4 fractions). K-Ar ages from fault system III range from 916.3 ± 18.6 Ma and 1384.7 ± 27.6 Ma (2 samples with 5 fractions, 1 sample with 4 fractions and 1 sample with one fraction). For fault system IV ages range from 953.1 ± 19.2 Ma to 1337.2 ± 26.7 Ma (2 samples with 5 fractions).
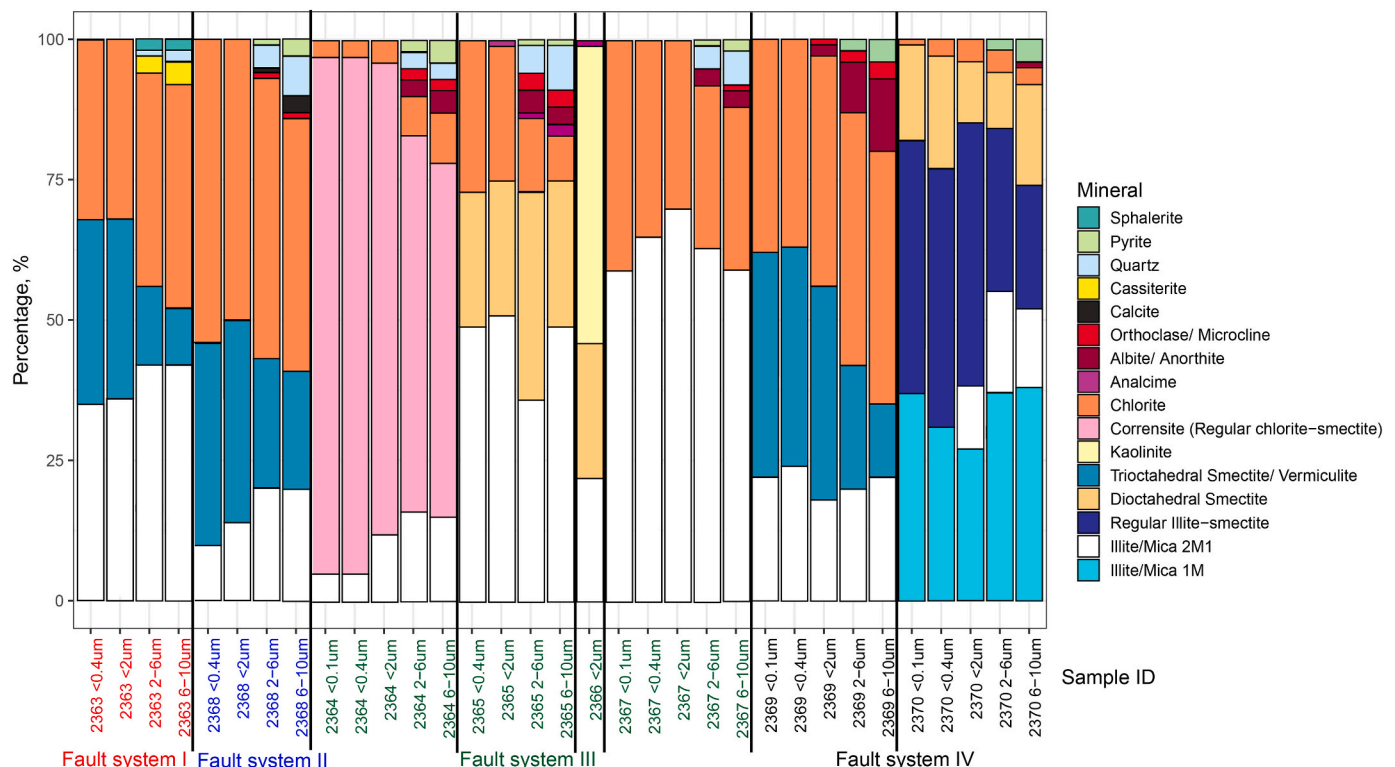
Fig. 10. XRD mineralogy data for the 33 separated clay-size fractions.
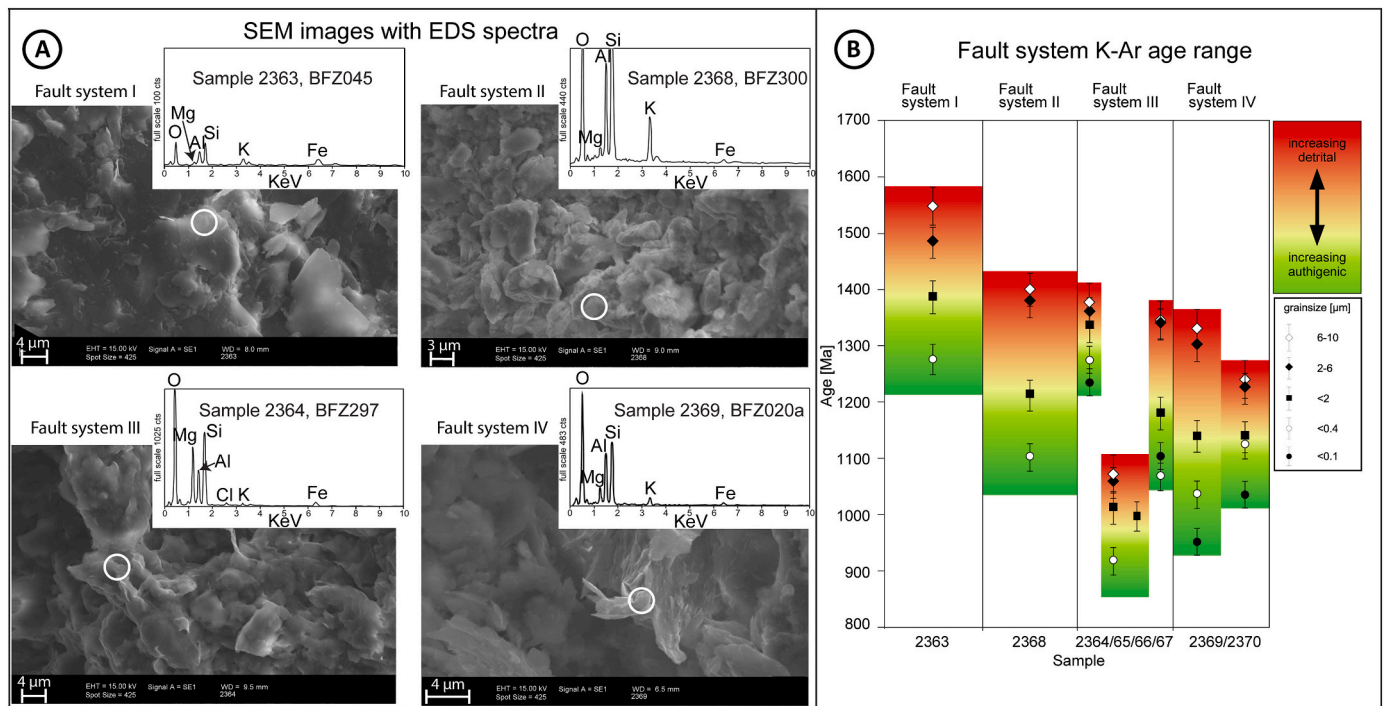
Fig. 11. A) SEM images from each fault system, including EDS spectra of the illite shown by the white circles. B) Comparison between our K-Ar age data for the different sample fractions and the four different fault systems. Assumed detrital contamination is visualised with a red and green colour scale. For the samples with less than 5 fractions the position and size of the coloured bracket is hypothetical. (For interpretation of the references to colour in this figure legend, the reader is referred to the web version of this article.)

7. Discussion

7.1. Age results interpretation

In this study we rely on the "Age Attractor Model" proposed by Torgersen et al. (2015) and Viola et al. (2016) to interpret the obtained age results. According to this model, the amount of old and inherited protolithic clay in a fault gouge decreases with the decreasing grain size of the dated fraction compared to the amount of authigenic and synkinematic clay, which instead increases with decreasing grain size. Thus, the coarsest sample fractions may contain relatively large amounts of old protolithic clay and the intermediate fractions a mixture of protolithic and authigenic minerals, such that dates do not necessarily reflect the timing of fault initial slip or reactivation. Instead, although even the finest fractions of illite may be variably contaminated by the host rock or may have experienced some degree of partial overprinting and resetting by younger tectonic and thermal events, many studies have shown that the finest illite sample fractions (< 0.1 μm or finer) yield a quite reliable record of the timing of the last brittle faulting event recorded by the fault (Viola et al., 2013, 2016; Torgersen and Viola, 2014; Mancktelow et al., 2015; Aldega et al., 2019; Scheiber et al., 2019; Curzi et al., 2020a; Curzi et al., 2020b; Tartaglia et al., 2020). Due to the clear observed trend of decreasing age with decreasing grain size within our data (Fig. 11B), we thus discuss and focus our interpretations on the results from the finest and geologically most meaningful fractions.

Based on the current understanding of the thermal development of the Olkiluoto area (Aaltonen et al., 2016), significant ^{40}Ar diffusion by a post-faulting thermal overprint up to 300 °C is unlikely (Akker et al., 2021), making the finest fractions even more reliable time markers. Their ages, however, need to be considered as only a maximum age of faulting because they may still contain varying amounts of inherited protolithic K-bearing phases that can influence the apparent age. Only if all K-Ar ages obtained from one sample are statistically identical for all dated grain size fractions, it is possible to assume that the age of the finest fraction as well as of all other fractions represents the true age of

the last recorded faulting event (Torgersen et al., 2015).

Out of the eight analysed fault rock samples, we could date the <0.1 μm fraction only from four samples: samples 2364 and 2367 from Fault system III and samples 2369 and 2370 from Fault system IV (Fig. 11B). A < 0.4 μm fraction was extracted and dated instead from three of the samples: sample 2363 from Fault system I, sample 2368 from Fault system II and sample 2365 from Fault system III (Fig. 11B). The smallest dated fraction for sample 2367 from Fault system III is <2 μm (Figs. 11B; 12; Table 3). The ages yielded by these clay fractions are listed in Table 4. The results thus only loosely constrain a K-Ar age of 1.28 Ga for sample 2363 from Fault system I fault zone BFZ045 (< 0.4 μm) and a somewhat younger K-Ar age of 1.10 Ga for sample 2368 from Fault system II fault zone BFZ300 (< 0.4 μm). Results are instead more indicative and reliable for Fault system III, where K-Ar ages, between 1.24 and 0.92 Ga from BFZ084 (sample 2367) and BFZ297 (samples 2364, 2365 and 2366) were obtained from <0.1 μm to <2 μm fractions. For Fault system IV we managed to also obtain two ages from the <0.1 μm fraction, indicating a last recorded slip event at 0.95 Ga and 1.04 Ga for fault zones BFZ020a (sample 2369) and BFZ020b (sample 2370), respectively.

Our K-Ar age results define a wide spread of overlapping ages (Table 3; Fig. 11B). Nevertheless, when assessing only the results from same fractions of different samples and from the finest clay fractions, a few trends do emerge (Table 4; Fig. 11B). The 1.28 Ga age for the <0.4 μm fraction from Fault system I is consistent with the result from the same fraction from Fault system III sample 2364. In addition, a 1.24 Ga K-Ar age was also determined for the <0.1 μm fraction from Fault system III sample 2364 which we interpret as the approximate age for a faulting event that affected Fault systems I and III. The 1.10 Ga K-Ar age for the <0.4 μm fraction from Fault system II sample 2368 is consistent with the results from the <0.1 μm and < 0.4 μm fractions of sample 2367 from Fault system III, which also record ages around 1.10 Ga. The determined 1.04 Ga K-Ar age for the <0.1 μm fraction of sample 2370 is the oldest age we register from Fault system IV. Despite the minor inconsistency between the finest fraction ages from samples 2367, 2368 and 2370, we

Table 3
K-Ar data.

Sample ID [μm]	Brittle deformation zone (fault system)	K [%]	Rad. ^{40}Ar [mol/g]	Rad. ^{40}Ar [%]	Age [Ma]	Error [Ma]
2363 < 0.4	BFZ045 (I)	3.61	1.1617E-08	99.14	1275.9	26.4
2363 < 2	BFZ045	3.63	1.3093E-08	98.90	1383.2	27.8
2363 2–6	BFZ045	3.95	1.5826E-08	99.65	1487.2	30.2
2363 6–10	BFZ045	3.64	1.5499E-08	99.65	1549.7	31.7
2368 < 0.4	BFZ300 (II)	1.38	3.6374E-09	98.81	1102.4	23.4
2368 < 2	BFZ300	1.57	4.7255E-09	99.12	1215.8	24.4
2368 2–6	BFZ300	2.17	7.8747E-09	99.59	1389.1	28.2
2368 6–10	BFZ300	2.18	8.0047E-09	99.56	1400.5	29.2
2364 < 0.1	BFZ297 (III)	1.81	5.5813E-09	91.05	1237.3	24.7
2364 < 0.4	BFZ297	1.67	5.3544E-09	98.39	1272.6	25.5
2364 < 2	BFZ297	2.18	7.5526E-09	98.54	1344.7	27.1
2364 2–6	BFZ297	2.35	8.3070E-09	99.12	1363.8	27.3
2364 6–10	BFZ297	2.24	8.0918E-09	99.21	1384.7	27.6
2365 < 0.4	BFZ297 (III)	3.65	7.5587E-09	95.67	916.3	18.6
2365 < 2	BFZ297	4.07	9.5792E-09	97.04	1011.8	20.3
2365 2–6	BFZ297	4.53	1.1417E-08	98.90	1065.9	21.7
2365 6–10	BFZ297	4.39	1.1160E-08	98.89	1072.8	21.9
2366 < 2	BFZ297 (III)	2.64	6.0272E-09	96.90	988.4	19.8
2367 < 0.1	BFZ084 (III)	3.95	1.0454E-08	97.30	1105.7	22.4
2367 < 0.4	BFZ084	3.86	9.8483E-09	97.34	1075.7	21.7
2367 < 2	BFZ084	4.53	1.3218E-08	98.17	1188.6	23.7
2367 2–6	BFZ084	4.50	1.5673E-08	99.19	1349.7	27.6
2367 6–10	BFZ084	4.38	1.5211E-08	99.43	1346.9	27.7
2369 < 0.1	BFZ20a (IV)	2.30	5.0096E-09	91.12	953.1	19.2
2369 < 0.4	BFZ20a	2.67	6.5510E-09	97.72	1044.4	20.9
2369 < 2	BFZ20a	2.62	7.2746E-09	98.42	1145.9	22.9
2369 2–6	BFZ20a	2.59	8.5785E-09	99.37	1302.5	26.2
2369 6–10	BFZ20a	2.55	8.7699E-09	99.53	1337.7	26.7
2370 < 0.1	BFZ20b (IV)	6.28	1.5273E-08	97.36	1037.4	20.8
2370 < 0.4	BFZ20b	6.29	1.7152E-08	98.03	1130.6	22.8
2370 < 2	BFZ20b	6.52	1.8086E-08	98.36	1145.1	22.9
2370 2–6	BFZ20b	6.24	1.9002E-08	99.71	1226.1	24.5
2370 6–10	BFZ20b	6.13	1.8992E-08	99.77	1241.6	24.8

interpret these three age results as representing the same faulting event affecting Fault system II, III and IV between 1.1 and 1.0 Ga. The grain size of finest dated fractions of samples 2365 and 2366 of Fault system III and sample 2369 of Fault system IV varies between <0.1 μm and 2 μm,

but all record ages younger than 1.0 Ga. The sample 2369 < 0.1 μm fraction from Fault system IV records a K-Ar age of 0.95 Ga while the <0.4 μm fraction of sample 2365 from Fault system III registers an age of 0.92 Ga and the <2 μm fraction of sample 2366 from Fault system III an age of 0.98 Ga. We interpret these age results as broadly defining a faulting event that affected Fault system III and IV roughly 0.95 Ga ago.

Our ages agree to some extent with the results of previous radiometric K-Ar studies from Olkiluoto by Viola et al. (2011b) and Mänttäri et al. (2007b) (Table 4). We note, however, that the study by Mänttäri et al. (2007b) only dated 2 μm fraction, making it difficult for a straight comparison with the ages of our dated finer fractions. This notwithstanding, as a whole the age data define four different faulting events (Fig. 13), which, although only loosely constrained from an absolute time perspective, are rather consistent with the independent structural and geological constraints highlighted above: (1) A faulting event at ca. 1.3–1.2 Ga, responsible for Fault system I and Fault system III. This deformation stage is the only episode recorded by the dated samples of Fault system I. (2) A faulting event at 1.1–1.0 Ga, which is recorded in Fault system II, III and IV. (3) A faulting event at c 0.97–0.87 Ga, which is recorded by Fault system III and Fault system IV. (4) A significantly younger event at ca. 0.55 Ga, only recorded by Fault system IV (Mänttäri et al., 2007b; Viola et al., 2011b). Despite minor inconsistencies between the grain size of the dated finest clay fractions of the different samples and some variations of the age results, the identified clusters and general trends of the available radiometric age data outline possible faulting episodes that give and find further support in the interpretation of the structural geological tunnel mapping data (Fig. 8A-F). Fig. 11B visualizes all our age data according to the different fault systems, highlighting the overlaps of the K-Ar data and related uncertainties of our interpretations.

7.2. Evolution of the fault complex of Olkiluoto

Based on the presented structural data, we can define four distinct brittle fault systems at Olkiluoto. Their relative age and kinematics have been determined by the characterization of representative fault zones. Due to the internal consistency of these datasets in terms of geological attributes, geometry, kinematics, and relative age relationships between specific types of faults, we consider the reconstructed fault systems and their relative age relationships as reliable and representative of the overall geological framework of Olkiluoto. Importantly, based on the orientation of the modelled fault zones in Aaltonen et al. (2016), 94% of the faults of the studied database fit with one of the four defined fault systems, indicating that our structural classification is well representative of the entire Olkiluoto fault complex. In the following we integrate our structural constraints with the new geochronological K-Ar data to constrain the initial formation of the fault systems and their selective reactivation during specific later tectonic events (Fig. 14).

Brittle deformation in Olkiluoto was preceded by a long history of ductile deformation that created heterogeneous migmatitic rocks with pre-existing planes of weaknesses that, to a varying degree, steered the initial development of different fault systems. Indeed, a complex tectonic history for the Olkiluoto site is suggested by the many fault rock types associated with the different fault systems and by the multiple generations of fault products within individual fault zones (see also Marchesini et al., 2019; Marchesini et al., 2022; Prando et al., 2019). This structural complexity is corroborated by our new K-Ar age results, which reveal and date multiple brittle events. Unfortunately, when dealing with such long deformation histories (implying several reactivation episodes) it is difficult to establish the age of initial nucleation and localisation of a fault system, and, therefore, to confidently interpret all the obtained radiometric results. In fact, as only maximum ages of deformation, even the reported ages of the finest fractions may be misleading as they may result from processes of partial resetting due to multiple mechanical reactivations of the dated fault system and fluid-rock interaction (see Zwingmann et al., 2019). Additionally, our

Fault system K–Ar ages
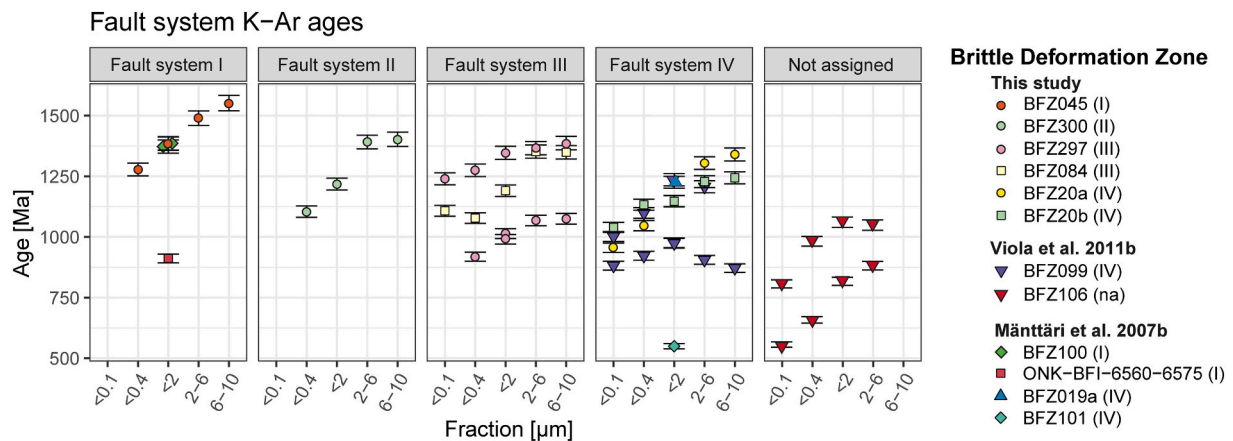
Fig. 12. K-Ar age data for 33 different clay fractions from the eight dated samples, consistently indicating a decrease in age with decreasing grain sizes. The analyses are classified based on the fault system the dated fault belongs to. For comparison, results from two earlier geochronology studies from Olkiluoto are included (Mänttäri et al., 2007b; Viola et al., 2011b).

Table 4

Analysed K-Ar ages for the finest illite clay size fractions. Results of previously published K-Ar studies from Olkiluoto by Mänttäri et al. (2007b) and Viola et al. (2011b) are listed in the lower part of the table.

Sample ID [μm]	Age [Ma]	Brittle fault zone (Fault system)	Sample description
2363 < 0.4	1275.9 ± 26.4	BFZ045 (I)	Brecciated fault core
2368 < 0.4	1102.4 ± 23.4	BFZ300 (II)	Clay bearing fault rock
2364 < 0.1	1237.3 ± 24.6	BFZ297 (III)	Brecciated fault core
2365 < 0.4	916.3 ± 18.6	BFZ297 (III)	Clay bearing fault rock
2366 < 2	988.4 ± 19.8	BFZ297 (III)	Illite-bearing breccia from fault core
2367 < 0.1	1105.7 ± 22.4	BFZ084 (III)	Clay-bearing fault rock from core
2369 < 0.1	953.1 ± 19.2	BFZ020a (IV)	Clay bearing fault rock
2370 < 0.1	1037.4 ± 20.1	BFZ020b (IV)	Clay bearing fault rock

Previously published age data				
Reference	Sample ID [μm]	Age [Ma]	Brittle fault zone (Fault system)	Sample description
Mänttäri et al., 2007b	872 < 2	912 ± 18.2	ONK-BFI-6560-6575 (I)	Breccia and clay
	874 < 2	1385 ± 27.4	BFZ100 (I)	Breccia and greenish/black clay
	875 < 2	1373 ± 27.2	BFZ100 (I)	Fault gouge/clay
	876 < 2	1225 ± 24.4	BFZ019a (IV)	Clay
Viola et al., 2011b	873 < 2	550 ± 10.9	BFZ101 (IV)	Breccia and greenish clay
	1270 < 0.1	886 ± 18.3	BFZ099 (IV)	Black clayish gouge
	1271 < 0.1	1006 ± 20.5	BFZ099 (IV)	Greyish banded gouge
	1260 < 0.1	811 ± 22.6	BFZ106 (n/a)	Gouge/ Ultracataclasite
	1261 < 0.1	561 ± 11.2	BFZ106 (n/a)	Gouge/clay-decorated planes

results indicate that some of the tectonic events in the area (Fig. 14) reactivated only part of the pre-existing fault systems within Olkiluoto, specifically fault structures oriented optimally for reactivation within the prevailing stress field. In the following, based on our new structural and geochronological data and previously published results, we interpret most of our new K-Ar data as representing structural reactivation of pre-existing fault systems. As shown by our structural constraints, however, fault zones in Olkiluoto do not contain much structural evidence attesting to the kinematics of superimposed reactivation episodes and at times only inferences can be made. In addition, some of the observed abutting and/or crosscutting relationships may be due to initial fault localization and do not necessarily express reactivation by later deformation episodes. Since original striations on slickensides and crosscutting relationships between fault systems are generally well preserved, we conclude that the amount of deformation during reactivations of previously formed fault systems has been relatively low and that reactivations may have been localised mainly within fault cores. Reactivation potential of individual faults or fault zones can also vary within a single fault system, as, in addition to geometric and dynamic criteria, the shear strength of individual faults can also be affected by the presence of mineralizations or by the presence of fluids, which may vary between faults in the same fault system. Thus, the validation of the model we propose, based on structural and K-Ar data would still require further detailed structural investigations of individual fault zones, associated with targeted additional dating and mineralogical studies.

These limitations and uncertainties notwithstanding, a theoretical model for the major phases of fault instability in Olkiluoto is presented in Fig. 14, where it is compared to recognised tectonic events previously proposed for southwestern Finland (Mattila and Viola, 2014). In the following, we discuss the details of the brittle evolution of the area.

7.2.1. Fault system I (1.79–1.2 Ga)

Fault system I, which we interpret as the oldest of the four fault systems documented in ONKALO™, displays the broadest documented range of fault products, including mylonite, pseudotachylite, cataclasite, breccia, quartz veins, synkinematic sulphide mineralizations, gouge and clay smears. The structures of Fault system I are sinistral strike-slip faults, approximately parallel to NNE–SSW trending, high-grade ductile shear structures (Skyttä and Torvela, 2018) that formed along the limbs of F_4 folds towards the end of D_4 (1.81 Ga ago, described in Aaltonen et al., 2016). At the tunnel scale, however, Fault system I structures cut the regional ductile structural grain.

The presence of N-S oriented mylonitic fabric is unique for Fault system I and only associated to the brittle structures of this system. We find these observations in line with the model by Prando et al. (2019), wherein the mylonitic phase is synchronous with the commencement of the brittle phase and cyclic quartz vein emplacement at the brittle-ductile transition zone (Fig. 14). Some of the hydrothermal alteration
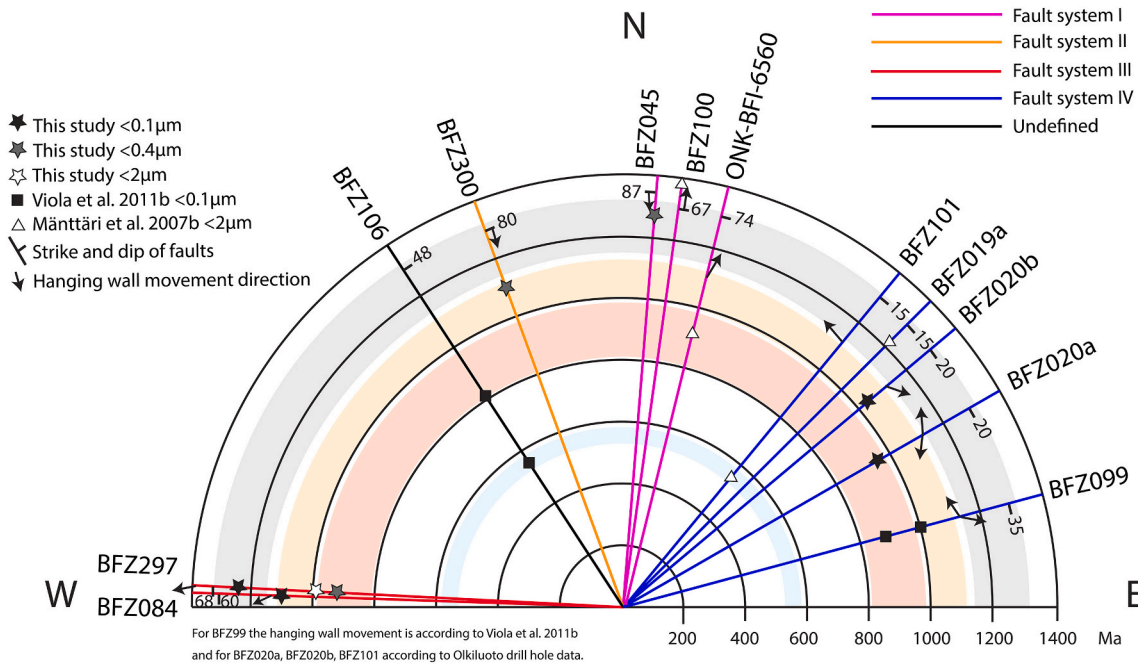
Fig. 13. K-Ar ages from Olkiluoto as a circular plot. The reported ages are from the finest clay fractions of all samples analysed to date from Olkiluoto (this study; Viola et al., 2011b and Mänttäri et al., 2007b). The colour-coded lines plot strike and fault systems of the dated fault. Ages are plotted on the strike lines of the faults they are associated with. Short black lines, numbers and arrows display, dip and hanging wall movement of the faults. The hanging wall movement is according to tunnel mapping data observations except for BFZ099 which is according to Viola et al., 2011b and for BFZ020a, BFZ020b and BFZ101 based on Olkiluoto drill hole data. The four different faulting episodes that emerge are highlighted by concentric arches with different colours. The plot is inspired by Davids et al. (2013) and Scheiber and Viola (2018).
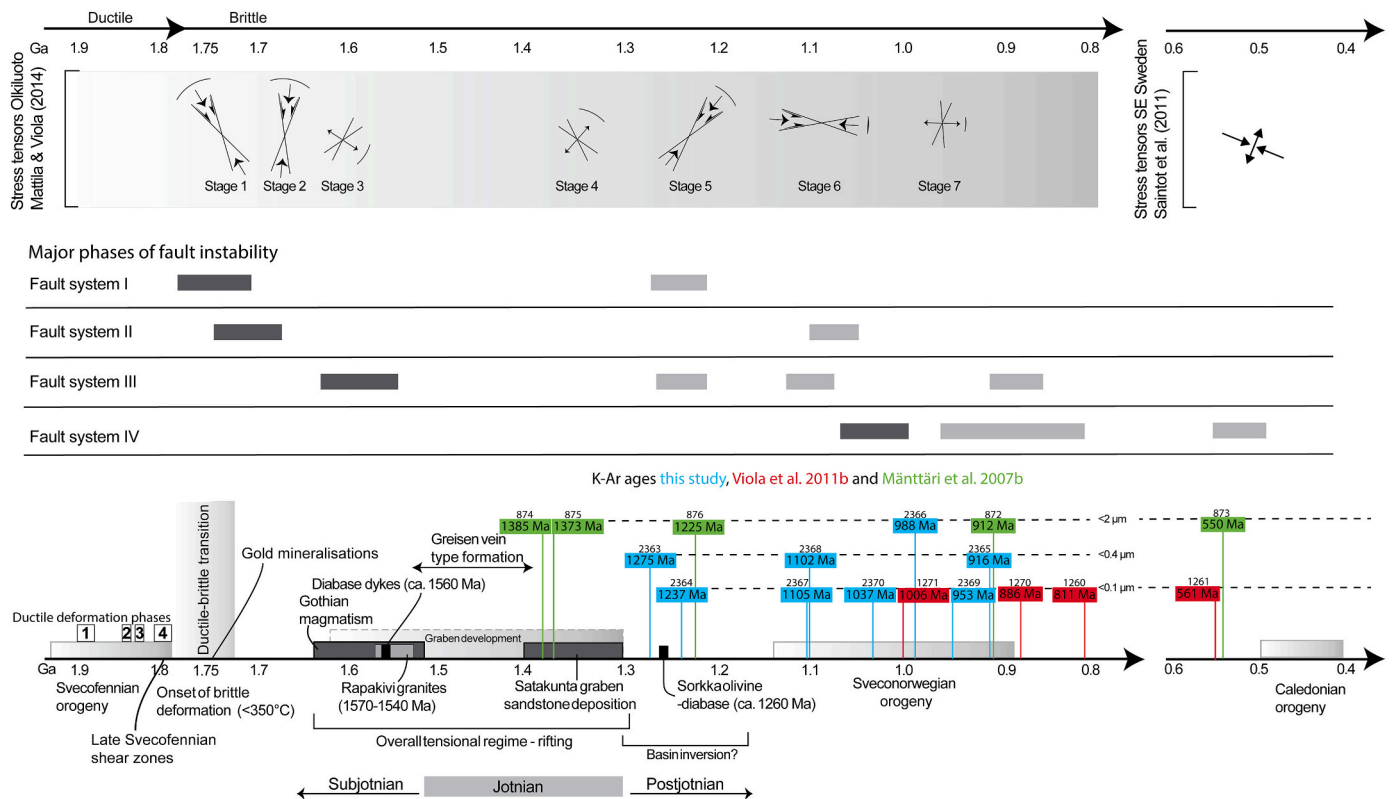
Fig. 14. Time-constrained model for the sequence of faulting events in Olkiluoto (dark-grey boxes represents initial faulting and light-grey boxes indicate structural reactivation). This interpretation is based on our structural geological observations, new and previously published K-Ar dates and other previously published studies from Olkiluoto (Mattila and Viola, 2014; Aaltonen et al., 2016; Marchesini et al., 2019; Prando et al., 2019). The faulting phases are compared with the interpreted stress tensor stages by Mattila and Viola (2014), Saintot et al. (2011) and the recognised tectonic events of southern Finland (Nironen, 2017). Figure modified after Mattila and Viola (2014).

and quartz veining processes studied in southwestern Finland have been found to be related to the late Svecofennian tectonics and the structurally controlled accumulation and percolation of metamorphic or magmatic fluids at the brittle-ductile transition (Saalmann, 2007; Saalmann et al., 2009). The source of the fluids that triggered the first embrittlement in Olkiluoto and emplaced the quartz veins in Fault system I are thus presumably connected to similar processes. Large scale N*E*-SW trending and steeply SE dipping late-Svecofennian ductile shear zones in southern Finland (Väisänen and Skyttä, 2007) show a long deformation history spanning from ductile to brittle deformation, with a progressive change towards more brittle deformation with time (Saalmann, 2007; Torvela et al., 2008). Many of these mylonitic shear zones were sinistrally reactivated during the final stages of the Svecofennian orogeny (Ploegsma and Westra, 1990; Pajunen, 2008). The sinistral reactivation event of the NE-SW trending shear zones is compatible with the formation of Fault system I during the late-Svecofennian, in response to paleostress conditions characterized by NW-SE to NNW-SSE shortening (Stage 1 in Mattila and Viola, 2014; Fig. 14). Hence, we consider the obtained 1.3–1.2 Ga K-Ar dates obtained from samples representative of Fault system I as a record of late reactivation of the fault system, which first formed at the transition from an overall ductile to brittle regime, occurring ca. 1.79–1.75 Ga ago in southern Finland (Torvela et al., 2008; Aaltonen et al., 2016).

This late reactivation of Fault system I, as constrained by the K-Ar data, postdates the extensional tectonic events during rapakivi intrusions and the formation of the Satakunta graben. Our obtained K-Ar ages of 1.3–1.2 Ga for Fault system I are matching closely however, with the ages of Postjotnian diabases (Suominen, 1991; Fig. 14). Mattila and Viola (2014) proposed the possibility that Postjotnian diabases formed in response to a phase of NE-SW compression (stage 5 in Mattila and Viola, 2014; Fig. 14). Geochronological ^{40}Ar-^{39}Ar K-feldspar and biotite results by Heeremans and Wijbrans (1999) from the Porkkala-Mäntsälä shear zone in southern Finland provided ages in the range of 1.3–0.95 Ga. These results show that late-Svecofennian shear zones were affected by brittle faulting and resetting of the K-Ar system during the time of intrusions of Postjotnian diabases and the Sveconorwegian orogeny (Fig. 14). Hence, we propose that the 1.3–1.2 Ga K-Ar results from Fault system I in Olkiluoto date local fault reactivation in response to the tectonic and thermal events related to the intrusion of Postjotnian diabases. Our K-Ar data do not register any later reactivations of Fault system I, although we note that this does not exclude that other reactivations may have occurred.

7.2.2. Fault system II (1.79–1.1 Ga)

Fault system II is composed of sub-vertical, NNW-SSE striking and steeply dipping dextral strike-slip faults that, as in the case of Fault system I, cut through the migmatitic gneiss foliation. They contain both quartz veins and evidence of hydrothermal alterations. Based on direct observations at the tunnel scale made on smaller-scale structures interpreted as Fault system II structures as well as on 3D modelling of the BFZ300 and BFZ346b fault zones, this fault system forms a NNW-SSE trending sub-vertical minor dextral fault set, interconnecting larger NN*E*-SSW striking sinistral Fault system I structures (Fig. 8D). Thus, the topological relationship between Fault system I and II differs from a synchronously formed and crosscutting conjugate fault pair, formed within a single stress field. Furthermore, the absence of mylonitic precursors in Fault system II indicates that Fault system I formed earlier and under more ductile conditions than Fault system II.

Microstructural, fluid inclusion and thermobarometry studies by Marchesini et al. (2019) and Prando et al. (2019) show that Fault system I and II both formed at the brittle-ductile transition zone (Fig. 14) through cyclic and fluid- induced slip at progressively lower temperature and pressure in an overall ductile regime. For fault zone BFZ300 (Fault system II), temperature and pressure conditions of the circulating fluids at the onset of localization have been constrained to 350 °C and 2.1 kbar (Marchesini et al., 2019), respectively, which is slightly lower

than the 450 °C, 3–3.5 kbar determined for the mylonitization of fault zone BFZ045 (Fault system I) (Prando et al., 2019). Thus, the model of distributed strike-slip shear by Schreurs (2003), is a reasonable analogue for the formation of Fault system I & II at mid-crustal levels. According to this model, the initial formation of Fault system I "master" faults would have caused local changes in the stress field that, with increasing strain, caused the formation of antithetic Fault system II "cross-faults", which interconnected the older, but still active, Fault system I structures. Marchesini et al. (2019) attributed the first development of the BFZ300 fault damage zone and the first generation of quartz to stage 1 by Mattila and Viola (2014), with paleostress conditions characterized by NW-SE to NNW-SSE compression, while the second generation of quartz in the core of BFZ300 emplaced under pure brittle conditions consistent with stage 2 of (Mattila and Viola, 2014; Fig. 14) of N-S to NN*E*-SSW transpressional compression. These results also suggest that the first embrittlement of Fault system I and II occurred in response to the same tectonic events during late-Svecofennian times, which would fit with the criteria of Schreurs (2003) for distributed strike-slip shear zones. A local clockwise rotation of the principal stress tensor in response to the formation of the Fault system I faults would also serve as a possible explanation for the accordingly rotated stage 2 stress tensor compared to stage 1 stress tensor in Mattila and Viola (2014).

Marchesini et al. (2019) identified possible later reactivations of fault zone BFZ300, suggesting an *E*-W compressional tectonic regime. The 1.1 Ga K-Ar age from our BFZ300 < 0.4 μm sample is also consistent with the suggested timing of stage 6 of Mattila and Viola (2014), characterized by E-W compression during the initial phases of the Sveconorwegian orogeny (Fig. 14), that initiated at 1.14 Ga ago (Bingen et al., 2008; Viola et al., 2011a). Based on crosscutting relationships, the formation of Fault system II predates the formation of Fault system III (Fig. 9A), which, in combination with the 1.2 Ga K-Ar ages of Fault system III (Fig. 13), indicate that Fault system II experienced reactivation after the formation of Fault system III. We acknowledge however, that the indistinct morphology of Fault system II and III sample materials (Fig. 11A) requires much caution when interpreting the obtained K-Ar ages.

7.2.3. Fault system III (1.6–0.9 Ga)

Fault system III contains E−W striking sub-vertical to moderately south-dipping dextral to oblique dextral/normal fault zones that are controlled by ductile precursors consisting of E−W trending and moderately south-dipping dextral ductile shear zones. According to Mänttäri et al. (2006), the shear zones were formed during deformation phase D$_3$, ca. 1.86–1.82 Ga ago (Fig. 14). Fault system III structures have not been the subject of detailed studies as those carried out on fault zones BFZ045, BFZ100 and BFZ300 (Pere, 2009; Marchesini et al., 2019; Prando et al., 2019) and therefore the evolution of this fault system remains poorly constrained.

Due to crosscutting relationships, differences in orientation and kinematics between fault zones and secondary structures (such as Riedel fractures) of the first two fault systems and Fault system III, Fault system III likely formed in response to a later tectonic event than those responsible for the first two systems. Although quartz and hydrothermal alterations are present in all the first three fault systems, due to the observed differences in filling mineralogy and hydrothermal alterations (Fig. 9A), we propose that the fluids that circulated in Fault system III have their origin from other sources than the fluids that caused the embrittlement and formation of quartz veins in Fault system I and II. Aaltonen et al. (2018) assigned the main hydrothermal episode in Olkiluoto to the intrusion of anorogenic rapakivi granites and mafic magmatism at around 1.5–1.6 Ga (Vaasjoki, 1996; Rämö and Haapala, 2005; Fig. 14). Furthermore, Aaltonen et al. (2018) linked the hydrothermal alteration products such as quartz and illite to processes associated with the migration of 200–300 °C hot fluids expelled from the crystallising rapakivi magma. Seismic surveys in Olkiluoto also indicate that rapakivi granites are found at >3 km depth below the island

(Kukkonen et al., 2010). Thereby, the rapakivi granites represent the most likely source for the hydrothermal fluids circulating in Fault system III.

However, the oblique dextral/normal kinematics for fault zones of the *E*-W striking Fault system III cannot be assigned to the NW-SE tensional or transtensional paleostress stage defined by Mattila and Viola (2014) for the latter stages of the Gothian orogeny (Åhall et al., 2000; Korja et al., 2001) and the intrusion of the rapakivi granites at around 1.5–1.6 Ga (Fig. 14). Thus, our hypothesis is that Fault system III formed in response to a previously undefined transtensional paleostress stage affecting the bedrock of southern Finland, possibly related to the episodic subduction and plate jamming associated with the Gothian orogeny (Åhall et al., 2000). A brittle tectonic event at 1.52 Ga has been constrained by means of Rb-Sr dating of fine-grained mineral slick-enfibres (illite and/or K-feldspar with calcite and/or albite) by Tillberg et al. (2020) in Forsmark, Sweden, although in association with kinematic data indicative of WSW-ENE compression. The K-Ar age results of Fault system III (Fig. 13), however, record later faulting events taking place between 1.2 and 0.9 Ga. Based on these results, Fault system III most likely reactivated simultaneously with the fault zones of Fault system I ca. at the time of Postjotnian diabase intrusions (Suominen, 1991), corresponding to the stage of NE-SW compression proposed in Mattila and Viola (Mattila and Viola, 2014; Fig. 14). The younger K-Ar ages of 1.1 and 0.9 Ga can be linked to further reactivations both at the onset and at the waning stage (orogenic collapse) of the Sveconorwegian orogeny (Fig. 14), with the initial phase characterized by E-W compression (stage 6 in Mattila and Viola, 2014) and the collapsing phase by E-W extension (stage 7 in Mattila and Viola, 2014).

7.2.4. Fault system IV (1.1–0.9 Ga)

Fault system IV contains low-angle fault zones that, in general, dip gently towards SE. Their kinematics are not univocal based on tunnel data, but drill hole observations suggest a thrust faulting-related origin. Fault system IV structures exploit planes of pre-existing weakness in the bedrock represented by lithological contacts between porphyritic granite rocks and weaknesses of the migmatitic foliation planes.

Structures of Fault system IV differ from the other fault systems since they lack evidence of hydrothermal alteration at temperatures higher than 200 °C, including quartz fillings and pervasive alteration of the host rock. The distinctly different mineralogical properties of Fault system IV, in combination with the observed crosscutting relationships to other fault systems (Fig. 9), leads us to interpret Fault system IV as the youngest of the four fault systems. The clustering of the oldest K-Ar ages of the Fault system IV samples around 1.04–1.0 Ga (Fig. 13) suggests that Fault system IV nucleated after the approximately 1.3–1.2 Ga event, which was recorded by both Fault system I and III. Slickenfibre Rb-Sr dating of the ZFM1203 structure in Forsmark (southeastern Sweden), with similar gently south dipping orientation, similar geological properties and kinematics as the structures of Fault system IV in Olkiluoto, yielded two different ages of 1.44 Ga and 1.07 Ga (Tillberg et al., 2020), with the latter fitting the K-Ar ages from Olkiluoto. In addition, Tillberg et al., 2021 also dated a vein mineralization sample from Forsmark to 1.1 Ga. These dating results support the paleostress analysis by Mattila and Viola (2014) where several stress tensors from Olkiluoto were interpreted to define a tectonic event with roughly E-W compression during the early stages of the Sveconorvegian orogeny (Fig. 14). The 0.87 Ga K-Ar age from brittle deformation zone BFZ099 (Viola et al., 2013; Fig. 13) can be interpreted as due to a reactivation of Fault system IV during the collapsing phase of the Sveconorwegian orogeny (Fig. 14). Elminen et al. (2018) obtained a 0.97 Ga K-Ar date from an extensional fracture from southern Finland that they also ascribed to the collapse of the Sveconorwegian orogeny. Previous studies (Elminen et al., 2018; Mänttäri et al., 2007b; Tillberg et al., 2020, 2021; Viola et al., 2011b) have, in addition, identified later reactivations that have been linked to

NW-SE to E-W crustal shortening during the early stages of the Caledonian orogeny (Viola et al., 2009; Saintot et al., 2011; Fig. 14).

8. Conclusions

Faults from Olkiluoto can be grouped into four distinct fault systems, each containing structural features that share similar tectonic histories and structural properties. From the oldest to the youngest fault systems are named as Fault systems I to IV. The chronological order and constraints on these four fault systems were determined based on their overall geological, geometric and kinematic characteristics and crosscutting relationships, whereas isotopic K-Ar data provided further constraints on the timing of formation and reactivation of the different fault systems (Fig. 14). In a broader context, the new data and interpretations presented above show that the bedrock in southern Finland experienced at least five major phases of deformation within the brittle regime spanning the period between ca. 1.75 Ga and 0.9 Ga. In addition, previous studies have identified possible further reactivation of Fault system IV structures, during the early stages of the Caledonian orogeny 0.5–0.4 Ga ago. The identified brittle deformation phases include:

1) Formation of N-S striking strike-slip faults at the brittle-ductile transition zone soon after the Svecofennian orogeny ca. 1.79–1.75 Ga ago in response to NW-SE to NNW-SSE compression, also causing brittle reactivation of late-Svecofennian NE-SW striking ductile shear zones.
2) Formation of E-W striking oblique dextral/normal faults in response to transtensional stresses tentatively associated to the tectonic events of the Gothian orogeny ca. 1.6 Ga ago.
3) NE-SW compression causing reactivation of the pre-existing fault systems at around 1.3–1.2 Ga, coeval with intrusion of olivine diabase sills.
4) Formation of low-angle thrust faults and reactivation of some of the pre-existing fault systems in response to E-W compression during the onset of the Sveconorwegian orogeny ca. 1.1–1.0 Ga ago.
5) E-W extension during the post-orogenic collapse of the Sveconorvegian orogen selectively reactivating some of the existing fault systems ca. 0.97–0.87 Ga ago.
6) NW-SE to E-W compression ca. 0.55 Ga ago prior to the Caledonian orogeny, reactivated low-angle thrust faults.

As such, our study yields new useful insights into the long, multistage and complex tectonic evolution of the bedrock in southern Finland and represents an example of general validity of how multidisciplinary studies make it possible to unravel even complex deformation histories of old crystalline terranes leading to time-constrained reconstructions.

Declaration of Competing Interest

The authors declare that they have no known competing financial interests or personal relationships that could have appeared to influence the work reported in this paper.

Appendix A. Supplementary description of analytical XRD and K-Ar methods

For clay polytype investigations the samples were lightly pressed into shallow stainless-steel holders for XRD analysis. Oriented samples were prepared by dispersing approximately 40 mg of material using ultrasonic agitation in approximately 5 ml of deionised water. The oriented samples were placed onto absorbent paper towels to remove excess glycerol on the backs of the samples before mounting onto 25 mm aluminium discs with double sided tape. XRD patterns were recorded with a PANalytical X'Pert Pro microprocessor-controlled diffractometer using Fe filtered Co Ka radiation, 0.25° divergence slit, 0.50° anti-scatter slit and X'Celerator fast Si strip detector. The diffraction patterns were recorded in steps of 0.016° 2 h with a 1 s counting time per step and logged to data files on a PC for analysis using the HighScore Plus and CSIRO XPLOT software.

The K-Ar measurements were performed according to the detailed explanations of the conventional K-Ar dating technique by Dalrymple and Lanphere (1969), Faure (1987) and Dickin (1995). Potassium content was determined by atomic absorption, (Varian Spectra AA 50), using Cs at 1000 ppm concentration for ionisation suppression. Argon isotopic determination was performed using a similar procedure to that described by Bonhomme et al. (1975). The sample was pre-heated under vacuum at 80 °C for several hours to reduce the amount of atmospheric Ar adsorbed onto the mineral surfaces during sample handling. Argon was extracted from the separated mineral fraction by fusing the sample within a vacuum line serviced by an on-line ^{38}Ar spike pipette. The isotopic composition of the spiked Ar was measured with a high sensitivity, on-line, VG3600 mass spectrometer. The ^{38}Ar spike was calibrated against a standard biotite, GA1550 (McDougall and Roksandic, 1974). Blanks for the extraction line and mass spectrometer were systematically determined and the mass discrimination factor was determined periodically by airshots.

Appendix B. XRD mineralogy data for the 33 separated clay-size fractions

Fault zone	Fault System	Sample ID (µm)	Quartz	Chlorite	Kaolinite	Illite/Mica 2 M1	Illite/Mica 1 M	Dioctahedral Smectite	Regular Illite-smectite	Trioctahedral Smectite/Vermiculite	Corrensite (Regular chlorite-smectite)	Albite/Anorthite	Orthoclase/Microcline	Pyrite	Sphalerite	Cassiterite	Analcime	Calcite
BFZ045	1	2363 < 0.4		32		35				33								
BFZ045	1	2363 < 2	<1	32		36				32								
BFZ045	1	2363 2–6	1	38		42				14					2	3		
BFZ045	1	2363 6–10	2	39		42				10					2	4		
BFZ300	2	2368 < 0.4		54		10				36								
BFZ300	2	2368 < 2	<1	50		14				36		<1	<1					
BFZ300	2	2368 2–6	4	50		20				23		1	1					1
BFZ300	2	2368 6–10	7	45		20				21		1	3					3
BFZ084	3	2367 < 0.1		41		59												
BFZ084	3	2367 < 0.4		35		65												
BFZ084	3	2367 < 2		30		71												
BFZ084	3	2367 2–6	4	29		63					3	<1	1					
BFZ084	3	2367 6–10	6	29		59					3	1	2					
BFZ297	3	2364 < 0.1		3		5					92							
BFZ297	3	2364 < 0.4		3		5					92							
BFZ297	3	2364 < 2		4		12					84		<1					
BFZ297	3	2364 2–6	3	7		16					67	3	2	2				
BFZ297	3	2364 6–10	3	9		15					63	4	2	4				
BFZ297	3	2365 < 0.4		27		49	24											
BFZ297	3	2365 < 2	<1	24		51	24					<1						1
BFZ297	3	2365 2–6	5	13		36	37					4	3	1				1
BFZ297	3	2365 6–10	8	8		49	26					3	3	1				2
BFZ297	3	2366 < 2	<1		53	22	24											1
BFZ20a	4	2369 < 0.1		38		22				40								
BFZ20a	4	2369 < 0.4		37		24				39		<1						

(continued)

Fault zone	Fault System	Sample ID (µm)	Quartz	Chlorite	Kaolinite	Illite/ Mica 2 M1	Illite/ Mica 1 M	Diocta hedral Smectite	Regular Illite-smectite	Trioctahedral Smectite/ Vermiculite	Corrensite (Regular chlorite-smectite)	Albite/ Anorthite	Orthoclase/ Microcline	Pyrite	Sphalerite	Cassiterite	Anal cime	Calcite
BFZ20a	4	2369 <2		41		18				38		2	1					
BFZ20a	4	2369 2–6	2	44		20				22		9	2	<1				
BFZ20a	4	2369 6–10	4	45		21				13		13	3					
BFZ20b	4	2370 <0.1		1			37	17	45									
BFZ20b	4	2370 <0.4		3			31	20	46									
BFZ20b	4	2370 <2		4		11	27	11	47									
BFZ20b	4	2370 2–6	2	4		18	37	10	29									
BFZ20b	4	2370 6–10	4	3		14	38	18	22			1					

References

Aaltonen, I., Engström, J., Front, K., Gehör, S., Kosunen, P., Kärki, A., Mattila, J., Paananen, M., Paulamäki, S., 2016. Geology of Olkiluoto. Posiva Report 2016–16. Posiva Oy, Eurajoki, p. 398.

Aaltonen, I., Front, K., Gehör, S., Sahlstedt, E., 2018. Hydrothermal Alteration of Bedrock at Olkiluoto, Posiva Report 2018–03. Posiva Oy, Eurajoki, p. 101.

Åhall, K.I., Connelly, J.N., Brewer, T.S., 2000. Episodic rapakivi magmatism due to distal orogenesis?: Correlation of 1.69 - 1.50 Ga orogenic and inboard, "anorogenic" events in the Baltic Shield. Geology 28, 823–826. https://doi.org/10.1130/0091-7613 (2000)28<823:ERMDTD>2.0.CO;2.

Akker, I.V., Berger, A., Zwingmann, H., Todd, A., Schrank, C.E., Jones, M.W.M., Kewish, C.M., Schmid, T.C., Herwegh, M., 2021. Structural and chemical resetting processes in white mica and their effect on K-Ar data during low temperature metamorphism. Tectonophysics 800, 228708. https://doi.org/10.1016/j.tecto.2020.228708.

Aldega, L., Viola, G., Casas-Sainz, A., Marcén, M., Román-Berdiel, T., van der Lelij, R., 2019. Unraveling multiple thermotectonic events accommodated by crustal-scale faults in Northern Iberia, Spain: insights from K-Ar dating of clay Gouges. Tectonics 38, 3629–3651. https://doi.org/10.1029/2019TC005585.

Fault slip analysis and palaeostress reconstruction. In: Angelier, J., Hancock, P.L. (Eds.), 1994. Continental Deformation, 1994. Pergamon, New York, pp. 53–100.

Barton, C.A., Zoback, M.D., Moos, D., 1995. Fluid flow along potentially active faults in crystalline rock. Geology 23, 683–686.

Bense, V.F., Gleeson, T., Loveless, S.E., Bour, O., Scibek, J., 2013. Fault zone hydrogeology. Earth Sci. Rev. 127, 171–192. https://doi.org/10.1016/j.earscirev.2013.09.008.

Bingen, B., Nordgulen, O., Viola, G., et al., 2008. A four-phase model for the Sveconorwegian orogeny, SW Scandinavia. Nor. Geol. Tidsskr. 88, 43.

Bogdanova, S., Gorbatschev, R., Skridlaite, G., Soesoo, A., Taran, L., Kurlovich, D., 2015. Trans-Baltic Palaeoproterozoic correlations towards the reconstruction of supercontinent Columbia/Nuna. Precambrian Res. 259, 5–33. https://doi.org/10.1016/j.precamres.2014.11.023.

Bonhomme, M.G., Thuizat, R., Winckler, R., Pinault, Y., Wendling, R., Clauer, N., 1975. Méthode de datation potassium-argon. Appareillage et Technique. 53.

Brace, W.F., 1980. Permeability of crystalline and argillaceous rocks. Int. J. Rock Mech. Min. Sci. Geomech. 17, 241–251. https://doi.org/10.1016/0148-9062(80)90807-4.

Curzi, M., Aldega, L., Bernasconi, S.M., Berra, F., Billi, A., Boschi, C., Franchini, S., Van der Lelij, R., Viola, G., Carminati, E., 2020a. Architecture and evolution of an extensionally-inverted thrust (Mt. Tancia Thrust, Central Apennines): geological, structural, geochemical, and K–Ar geochronological constraints. J. Struct. Geol. 136, 104059 https://doi.org/10.1016/j.jsg.2020.104059.

Curzi, Manuel, Billi, A., Carminati, E., Rossetti, F., Albert, R., Aldega, L., Cardello, G.L., Conti, A., Gerdes, A., Smeraglia, L., Van der Lelij, R., Vignaroli, G., Viola, G., 2020b. Disproving the presence of paleozoic-triassic metamorphic rocks on the Island of Zannone (Central Italy): implications for the early stages of the Tyrrhenian-Apennines tectonic evolution. Tectonics 39, e2020TC006296. https://doi.org/10.1029/2020TC006296.

Dalrymple, G.B., Lanphere, M.A., 1969. Potassium-Argon Dating. W. H. Freeman, San Francisco, p. 258.

Davids, C., Wemmer, K., Zwingmann, H., Kohlmann, F., Jacobs, J., Bergh, S.G., 2013. K–Ar illite and apatite fission track constraints on brittle faulting and the evolution of the northern Norwegian passive margin. Tectonophysics 608, 196–211. https://doi.org/10.1016/j.tecto.2013.09.035.

Dickin, A.P., 1995. Radiogenic Isotope Geology, , Second edition509.

Ehlers, C., Lindroos, A., Selonen, O., 1993. The late Svecofennian granite-migmatite zone of southern Finland—a belt of transpressive deformation and granite emplacement. Precambrian Research Baltic Shield 64, 295–309. https://doi.org/10.1016/0301-9268(93)90083-E.

Eklund, O., Shebanov, A.D., 1999. The origin of rapakivi texture by sub-isothermal decompression. Precambrian Res. 95, 129–146. https://doi.org/10.1016/S0301-9268(98)00130-2.

Elminen, T., Zwingmann, H., Kaakinen, A., 2018. Constraining the timing of brittle deformation and sedimentation in southern Finland: Implications for Neoproterozoic evolution of the eastern Fennoscandian shield. Precambrian Res. 304, 110–124. https://doi.org/10.1016/j.precamres.2017.10.014.

Engström, J., 2013. Geological ductile deformation mapping at the Olkiluoto Site, Eurajoki, Finland. In: Posiva Working Report 2013–62. Posiva Oy, Eurajoki, p. 68.

Faure, G., 1987. Principles of Isotope Geology. John Wiley and Sons, New York, p. 589.

Fransson, Å., Viola, G., 2021. Bentonite rock interaction experiment: a hydro-structural-mechanical approach. Eng. Geol. 281, 105985 https://doi.org/10.1016/j.enggeo.2020.105985.

Fransson, Å., Lönnqvist, M., Viola, G., 2019. Rock mechanical modelling of the Bentonite Rock Interaction Experiment, Äspö Hard Rock Laboratory, Sweden. Int. J. Rock Mech. Min. Sci. 113, 255–267. https://doi.org/10.1016/j.ijrmms.2018.10.017.

Gaál, G., Gorbatschev, R., 1987. An outline of the precambrian evolution of the baltic shield. Precambrian Res. 17, 149–159.

Gorbatschev, R., Bogdanova, S., 1993. Frontiers in the Baltic Shield. Precambrian Research Baltic Shield 64, 3–21. https://doi.org/10.1016/0301-9268(93)90066-B.

Haines, S.H., van der Pluijm, B.A., 2008. Clay quantification and Ar-Ar dating of synthetic and natural gouge: application to the Miocene Sierra Mazatán detachment fault, Sonora, Mexico. J. Struct. Geol. 30, 525–538. https://doi.org/10.1016/j.jsg.2007.11.012.

Heeremans, M., Wijbrans, J., 1999. Late Proterozoic tectonic events in southern Finland, constrained by40Ar/39Ar incremental heating and single spot fusion experiments on K-feldspars. Terra Nova 11, 216–222. https://doi.org/10.1046/j.1365-3121.1999.00250.x.

Heilimo, E., 2005. Vehmaan Rapakiven Kontaktimetamorfoosi. Master's Thesis (in Finnish). Department of Geology, University of Turku, Finland.

Hess, J.C., Lippolt, H.J., 1994. Compilation of K-Ar measurements on HD-B1 standard biotite. In: Odin, G.S. (Ed.), Phanerozoic time scale, Bull. Lias. Inform., IUGS subcom. Geochronol., 12, Paris, pp. 19–23.

Hoek, E., Brown, E.T., 1980. Underground Excavations in Rock, Rev. ed. Institution of Mining and Metallurgy, London.

Hudson, J.A., Cosgrove, J.W., Kemppainen, K., Johansson, E., 2011. Faults in crystalline rock and the estimation of their mechanical properties at the Olkiluoto site, western Finland. Eng. Geol. 117, 246–258. https://doi.org/10.1016/j.enggeo.2010.11.004.

Kärki, A., Paulamäki, S., 2006. Petrology of Olkiluoto. Posiva report 2006–02. Posiva Oy, Eurajoki, p. 87.

Kohonen, J., Rämö, O.T., 2005. Chapter 13 Sedimentary rocks, diabases, and late cratonic evolution. In: Lehtinen, M., Nurmi, P.A., Rämö, O.T. (Eds.), Developments in Precambrian Geology, Precambrian Geology of Finland Key to the Evolution of the Fennoscandian Shield. Elsevier, pp. 563–603. https://doi.org/10.1016/S0166-2635(05)80014-3.

Kohonen, J., Pihlaja, P., Kujala, H., Marmo, J., 1993. Sedimentation of the Jotnian Satakunta sandstone, western Finland. Bull. Geol. Surv. Finland 369, 35.

Korja, A., Heikkinen, P., Aaro, S., 2001. Crustal structure of the northern Baltic Sea palaeorift. Tectonophysics 331, 341–358. https://doi.org/10.1016/S0040-1951(00)00290-0.

Kralik, M., Clauer, N., Holnsteiner, R., Huemer, H., Kappel, F., 1992. Recurrent fault activity in the Grimsel Test Site (GTS, Switzerland): revealed by Rb-Sr, K-Ar and tritium isotope techniques. J. Geol. Soc. 149, 293–301. https://doi.org/10.1144/gsjgs.149.2.0293.

Kukkonen, I., Heikkinen, P., Paananen, M., Elo, S., Paulamäki, S., Heinonen, S.E., Laitinen, J., Finland, H.W.G. of the G.S. of, 2010. HIRE Seismic Reflection Survey in the Olkiluoto Area, Western Finland.

Kurhila, M., Vaasjoki, M., Mänttäri, I., Rämö, T., Nironen, M., 2005. U-Pb ages and Nd isotope characteristics of the lateorogenic, migmatizing microcline granites in southwestern Finland. Bull. Geol. Soc. Finl. 77, 105–128. https://doi.org/10.17741/bgsf/77.2.002.

Kurhila, M., Andersen, T., Rämö, O.T., 2010. Diverse sources of crustal granitic magma: Lu-Hf isotope data on zircon in three Paleoproterozoic leucogranites of southern Finland. Lithos 115, 263–271. https://doi.org/10.1016/j.lithos.2009.12.009.

Lahtinen, R., Korja, A., Nironen, M., 2005. Chapter 11 Paleoproterozoic tectonic evolution. In: Developments in Precambrian Geology. Elsevier, pp. 481–531. https://doi.org/10.1016/S0166-2635(05)80012-X.

Lahtinen, R., Korja, A., Nironen, M., Heikkinen, P., 2009. Palaeoproterozoic accretionary processes in Fennoscandia. Geol. Soc. Lond., Spec. Publ. 318, 237–256. https://doi.org/10.1144/SP318.8.

Larson, S.Å., Tullborg, E.-L., Cederbom, C., Stiberg, J.-P., 1999. Sveconorwegian and Caledonian foreland basins in the Baltic Shield revealed by fission-track thermochronology. Terra Nova 11, 210–215. https://doi.org/10.1046/j.1365-3121.1999.00249.x.

Mancktelow, N., Zwingmann, H., Campani, M., et al., 2015. Timing and conditions of brittle faulting on the Silltal-Brenner Fault Zone, Eastern Alps (Austria). Swiss J. Geosci. 108, 305–326. https://doi.org/10.1007/s00015-015-0179-y.

Mänttäri, I., Talikka, M., Paulamäki, S., Mattila, J., 2006. U-Pb Ages for Tonalitic Gneiss, Pegmatitic Granite, and Diabase Dyke, Olkiluoto Study Site, Eurajoki, SW Finland. Posiva Working report 2006–12. Posiva Oy, Eurajoki, p. 18.

Mänttäri, I., Aaltonen, I., Lindberg, A., 2007a. U-Pb Ages for Two Tonalitic Gneisses, Pegmatitic Granites, and K-Feldspar Porphyries, Olkiluoto Study Site, Eurajoki, SW Finland. Posiva Working report 2007–70. Posiva Oy, Eurajoki, p. 44.

Mänttäri, I., Mattila, J., Zwingmann, H., Todd, A.J., 2007b. Illite K-Ar dating of fault breccia samples from ONKALO underground research facility, Olkiluoto, Eurajoki, SW Finland. In: Posiva Working Report 2007–67. Posiva Oy, Eurajoki, p. 40.

Mänttäri, I., Pere, T., Engström, J., Lahaye, Y., 2010. U-Pb Ages for PGR Dykes, KFP, and Adjacent older Leucosomic PGRs from ONKALO Underground Research Facility, Olkiluoto, Eurajoki, SW Finland. Posiva Working Report 2010–31. Posiva Oy, Eurajoki, p. 52.

Marchesini, B., Garofalo, P.S., Menegon, L., Mattila, J., Viola, G., 2019. Fluid-mediated, brittle–ductile deformation at seismogenic depth – part 1: Fluid record and deformation history of fault veins in a nuclear waste repository (Olkiluoto Island, Finland). Solid Earth 10, 809–838. https://doi.org/10.5194/se-10-809-2019.

Marchesini, B., Menegon, L., Schwarz, G., Neff, C., Keresztes Schmidt, P., Garofalo, P.S., Hattendorf, B., Günther, D., Mattila, J., Viola, G., 2022. Strain-induced trace element mobility in a quartz-sulphide vein system: an example from the ONKALOTM spent nuclear fuel repository (Olkiluoto, SW Finland). J. Struct. Geol. 154, 104473 https://doi.org/10.1016/j.jsg.2021.104473.

Mattila, J., Tammisto, E., 2012. Stress-controlled fluid flow in fractures at the site of a potential nuclear waste repository, Finland. Geology 40, 299–302. https://doi.org/10.1130/G32832.1.

Mattila, J., Viola, G., 2014. New constraints on 1.7 Gyr of brittle tectonic evolution in southwestern Finland derived from a structural study at the site of a potential nuclear waste repository (Olkiluoto Island). J. Struct. Geol. 67, 50–74. https://doi.org/10.1016/j.jsg.2014.07.003.

McDougall, I., Roksandic, Z., 1974. Total fusion 40Ar/39Ar ages using Hifar reactor. J. Geol. Soc. Aust. 21, 81–89. https://doi.org/10.1080/00167617408728836.

McEwen, T., Aro, S., Kosunen, P., Mattila, J., Pere, T., Kapyaho, A., Hella, P., 2012. Rock suitability classification RSC 2012. Posiva Report 2012–24. Posiva Oy, Eurajoki, p. 220.

Moore, D.M., Reynolds, R.C., 1997. X-Ray Diffraction and the Identification and Analysis of Clay Minerals, 2nd ed. Oxford University Press, Oxford; New York.

Morris, A., Ferrill, D.A., Henderson, D.B., Morris, A., Ferrill, D.A., Henderson, D.B., 1996. Slip-tendency analysis and fault reactivation. Geology 24, 275–278. https://doi.org/10.1130/0091-7613(1996)024<0275.

Munier, R., 2006. Using observations in deposition tunnels to avoid intersections with critical fractures in deposition holes. In: SKB Report R06–54. Swedish Nuclear Fuel and Waste Management Co.

Nironen, M., 1997. The Svecofennian Orogen: a tectonic model. Precambrian Res. 86, 21–44. https://doi.org/10.1016/S0301-9268(97)00039-9.

Nironen, M. (Ed.), 2017. Bedrock of Finland at the Scale 1:1 000 000 - Major Stratigraphic Units, Metamorphism and Tectonic Evolution, Special Paper/Geological Survey of Finland. Geological Survey of Finland, Espoo.

Nordbäck, N., 2014. Tunnel Crosscutting Fractures (TCF) in ONKALO (chainage 0-4986). In: Posiva Working Report 2014–58. Posiva Oy, Eurajoki, p. 50.

Nordbäck, N., Engström, J., 2016. Outcome of geological mapping and prediction-outcome studies of ONKALO. In: Posiva Report 2016–14. Posiva Oy, Eurajoki, p. 124.

Nordbäck, N., Mattila, J., 2018. Brittle Fault Systems of the ONKALO Underground Research Facility. In: Posiva Working Report 2018–20. Posiva Oy, Eurajoki, p. 80.

Odin, G.S., 35 collaborators, 1982. Interlaboratory standards for dating purposes. In: Odin, G.S. (Ed.), Numerical Dating in Stratigraphy. Part 1. John Wiley and Sons, Chichester, pp. 123–148.

Pajunen, M. (Ed.), 2008. Tectonic Evolution of the Svecofennian Crust in Southern Finland -a Basis for Characterizing Bedrock Technical Properties, Special Paper 47. Geological Survey of Finland, Espoo.

Peacock, D.C.P., Nixon, C.W., Rotevatn, A., Sanderson, D.J., Zuluaga, L.F., 2017. Interacting faults. J. Struct. Geol. 97, 1–22. https://doi.org/10.1016/j.jsg.2017.02.008.

Pere, T., 2009. Fault-related Local Phenomena in the Bedrock of Olkiluoto. With Particular Reference to Fault Zone OL-BFZ100. No. 2009–125, Posiva Working Report 2009-125. Posiva Oy, Eurajoki, p. 98.

Ploegsma, M., Westra, L., 1990. The early Proterozoic Orijärvi triangle (Southwest Finland): a key area on the tectonic evolution of the Svecofennides. Precambrian Res. 47, 51–69. https://doi.org/10.1016/0301-9268(90)90030-T.

Prando, F., Menegon, L., Anderson, M.W., Marchesini, B., Mattila, J., Viola, G., 2019. Fluid-mediated, brittle-ductile deformation at seismogenic depth: Part II – stress history and fluid pressure variations in a shear zone in a nuclear waste repository (Olkiluoto Island, Finland). Solid Earth Discus. 1–41 https://doi.org/10.5194/se-2019-142.

Rämö, O.T., Haapala, I., 2005. Chapter 12 Rapakivi Granites. In: Lehtinen, M., Nurmi, P. A., Rämö, O.T. (Eds.), Developments in Precambrian Geology, Precambrian Geology of Finland Key to the Evolution of the Fennoscandian Shield. Elsevier, pp. 533–562. https://doi.org/10.1016/S0166-2635(05)80013-1.

Rämö, O.T., Mänttäri, I., 2015. Geochronology of the Suomenniemi rapakivi granite complex revisited: Implications of point-specific errors on zircon U-Pb and refined λ87 on whole-rock Rb-Sr. Bull. Geol. Soc. Finl. 87, 25–45. https://doi.org/10.17741/bgsf/87.1.002.

Saalmann, K., 2007. Structural control on gold mineralization in the Satulinmäki and Riukka prospects, Häme Schist Belt, southern Finland. Bull. Geol. Soc. Finland 79, 69–93. https://doi.org/10.17741/bgsf/79.1.004.

Saalmann, K., Mänttäri, I., Ruffet, G., Whitehouse, M.J., 2009. Age and tectonic framework of structurally controlled Palaeoproterozoic gold mineralization in the Häme belt of southern Finland. Precambrian Res. 174, 53–77. https://doi.org/10.1016/j.precamres.2009.06.005.

Saintot, A., Stephens, M.B., Viola, G., Nordgulen, 2011. Brittle tectonic evolution and paleostress field reconstruction in the southwestern part of the Fennoscandian Shield, Forsmark, Sweden. Tectonics 30, 1–36. https://doi.org/10.1029/2010TC002781.

Scheiber, T., Viola, G., 2018. Complex bedrock fracture patterns: a multipronged approach to resolve their evolution in space and time. Tectonics 37, 1030–1062. https://doi.org/10.1002/2017TC004763.

Scheiber, T., Viola, G., van der Lelij, R., Margreth, A., Schönenberger, J., 2019. Microstructurally-constrained versus bulk fault gouge K-Ar dating. J. Struct. Geol. 127, 103868 https://doi.org/10.1016/j.jsg.2019.103868.

Schreurs, G., 2003. Fault development and interaction in distributed strike-slip shear zones: an experimental approach. Geol. Soc. Lond., Spec. Publ. 210, 35–52. https://doi.org/10.1144/GSL.SP.2003.210.01.03.

Sibson, R.H., 1985. A note on fault reactivation. J. Struct. Geol. 7, 751–754. https://doi.org/10.1016/0191-8141(85)90150-6.

SKB, 2011. Long-Term Safety for the Final Repository for Spent Nuclear Fuel at Forsmark - Main Report of the SR-Site Project. Technical Report TR-11-01. Svensk Kärnbränslehantering AB, Stockholm.

Skyttä, P., Torvela, T., 2018. Brittle reactivation of ductile precursor structures: the role of incomplete structural transposition at a nuclear waste disposal site, Olkiluoto, Finland. J. Struct. Geol. 116, 253–259. https://doi.org/10.1016/j.jsg.2018.06.009.

Skyttä, P., Ovaskainen, N., Nordbäck, N., Engström, J., Mattila, J., 2021. Fault-induced mechanical anisotropy and its effects on fracture patterns in crystalline rocks. J. Struct. Geol. 146, 104304 https://doi.org/10.1016/j.jsg.2021.104304.

Steiger, R.H., Jäger, E., 1977. Subcommission on geochronology: Convention on the use of decay constants in geo- and cosmochronology. Earth Planet. Sci. Lett. 36, 359–362. https://doi.org/10.1016/0012-821X(77)90060-7.

Suominen, V., 1991. The chronostratigraphy of southwestern Finland: with special reference to Postjotnian and Subjotnian diabases. Geol. Surv. Finland Bull. 356, 100.

Tartaglia, G., Viola, G., Ceccato, A., Bernasconi, S., van der Lelij, R., Scheiber, T., 2020. Multiphase brittle tectonic evolution of the Mid-Norwegian margin, Central Norway, reconstructed by remote sensing, paleostress inversion and K-Ar fault rock dating. No. EGU2020-5438. In: Copernicus Meetings. https://doi.org/10.5194/egusphere-egu2020-5438.

Tillberg, M., Drake, H., Zack, T., Kooijman, E., Whitehouse, M.J., Åström, M.E., 2020. In situ Rb-Sr dating of slickenfibres in deep crystalline basement faults. Sci. Rep. 10 https://doi.org/10.1038/s41598-019-57262-5.

Tillberg, M., Drake, H., Zack, T., Hogmalm, J., Kooijman, E., Åström, M.E., 2021. Reconstructing craton-scale tectonic events via in situ Rb-Sr geochronology of poly-phased vein mineralization. Terra Nova 2021 (00), 1–9. https://doi.org/10.1111/ter.12542.

Torgersen, E., Viola, G., 2014. Structural and temporal evolution of a reactivated brittle-ductile fault - part I: fault architecture, strain localization mechanisms and deformation history. Earth Planet. Sci. Lett. 407, 205–220. https://doi.org/10.1016/j.epsl.2014.09.019.

Torgersen, E., Viola, G., Zwingmann, H., Harris, C., 2015. Structural and temporal evolution of a reactivated brittle-ductile fault - Part II: timing of fault initiation and reactivation by K-Ar dating of synkinematic illite/muscovite. Earth Planet. Sci. Lett. 410, 212–224. https://doi.org/10.1016/j.epsl.2014.09.051.

Torvela, T., Mänttäri, I., Hermansson, T., 2008. Timing of deformation phases within the South Finland shear zone, SW Finland. Precambrian Res. 160, 277–298. https://doi.org/10.1016/j.precamres.2007.08.002.

Tsukamoto, S., Tagami, T., Zwingmann, H., 2020. Direct dating of fault movement. In: Understanding Faults. Elsevier, pp. 257–282. https://doi.org/10.1016/B978-0-12-815985-9.00007-2.

Tuisku, P., Kärki, A., 2010. Metamorphic petrology of Olkiluoto. In: Posiva Working Report 2010–54. Posiva Oy, Eurajoki, p. 76.

Uysal, I.T., Delle Piane, C., Todd, A.J., Zwingmann, H., 2020. Precambrian faulting episodes and insights into the tectonothermal history of north Australia: microstructural evidence and K–Ar, 40Ar–39Ar, and Rb–Sr dating of syntectonic illite

from the intracratonic Millungera Basin. Solid Earth 11, 1653–1679. https://doi.org/10.5194/se-11-1653-2020.

Vaasjoki, M., 1996. Explanation to the geochronological map of Southern Finland: the development of the continental crust with special reference to the Svecofennian orogeny. Geol. Surv. Finland Rep. Investig. 135, 32p.

Väisänen, M., Skyttä, P., 2007. Late svecofennian shear zones in southwestern Finland. Gff 129, 55–64. https://doi.org/10.1080/11035890701291055.

Van Balen, R.T., Heeremans, M., 1998. Middle Proterozoic-early Palaeozoic evolution of central Baltoscandian intracratonic basins: evidence for asthenospheric diapirs. Tectonophysics 300, 131–142. https://doi.org/10.1016/S0040-1951(98)00237-6.

Viola, G., Venvik Ganerød, G., Wahlgren, C.H., 2009. Unraveling 1.5 Ga of brittle deformation history in the Laxemar-Simpevarp area, Southeast Sweden: a contribution to the Swedish site investigation study for the disposal of highly radioactive nuclear waste. Tectonics 28. https://doi.org/10.1029/2009TC002461.

Viola, G., Henderson, I.H.C., Bingen, B., Hendriks, B.W.H., 2011a. The Grenvillian–Sveconorwegian orogeny in Fennoscandia: Back-thrusting and extensional shearing along the "Mylonite Zone.". Precambrian Res. 189, 368–388. https://doi.org/10.1016/j.precamres.2011.06.005.

Viola, G., Mattila, J., Zwingmann, H., Todd, A., Raven, M., 2011b. Structural and K/Ar Illite geochronological constraints on the brittle deformation history of the Olkiluoto Region, Southwest Finland. In: Posiva Working Report 2011–37. Posiva Oy, Eurajoki, p. 170.

Viola, G., Zwingmann, H., Mattila, J., Käpyaho, A., 2013. K-Ar illite age constraints on the Proterozoic formation and reactivation history of a brittle fault in Fennoscandia. Terra Nova 25, 236–244. https://doi.org/10.1111/ter.12031.

Viola, G., Scheiber, T., Fredin, O., Zwingmann, H., Margreth, A., Knies, J., 2016. Deconvoluting complex structural histories archived in brittle fault zones. Nat. Commun. 7, 1–10. https://doi.org/10.1038/ncomms13448.

Viola, G., Torgersen, E., Mazzarini, F., Musumeci, G., van der Lelij, R., Schönenberger, J., Garofalo, P.S., 2018. New Constraints on the Evolution of the Inner Northern Apennines by K-Ar Dating of late Miocene-early Pliocene Compression on the Island of Elba, Italy. Tectonics 37, 3229–3243. https://doi.org/10.1029/2018TC005182.

Vrolijk, P., Pevear, D., Covey, M., LaRiviere, A., 2018. Fault gouge dating: history and evolution. Clay Miner. 53, 305–324. https://doi.org/10.1180/clm.2018.22.

Zwingmann, H., Mancktelow, N., 2004. Timing of Alpine fault gouges. Earth Planet. Sci. Lett. 223, 415–425. https://doi.org/10.1016/j.epsl.2004.04.041.

Zwingmann, H., Mancktelow, N., Antognini, M., Lucchini, R., 2010. Dating of shallow faults: New constraints from the AlpTransit tunnel site (Switzerland). Geology 38, 487–490. https://doi.org/10.1130/G30785.1.

Zwingmann, H., den Hartog, S.A.M., Todd, A., 2019. The effect of sub-seismic fault slip processes on the isotopic signature of clay minerals – Implications for K-Ar dating of fault zones. Chem. Geol. 514, 112–121. https://doi.org/10.1016/j.chemgeo.2019.03.034.